Delft University of Technology

Influence of surface roughness on the mode II fracture toughness and fatigue resistance of bonded composite-to-steel joints

Feng, Weikang; Arouche, Marcio Moreira; Pavlovic, Marko

Important note
To cite this publication, please use the final published version (if applicable).
Please check the document version above.

Influence of surface roughness on the mode II fracture toughness and fatigue resistance of bonded composite-to-steel joints

Weikang Feng, Marcio Moreira Arouche, Marko Pavlovic [*]

Faculty of Civil Engineering and Geoscience, Delft University of Technology, 2600AA, Delft, the Netherlands

A B S T R A C T

Hybrid bi-material concepts in engineering structures where fibre-polymer composites are used together with steel structural members have potential to reduce material usage, extend fatigue life and improve structural reliability. The bond performance of the bi-material composite-to-steel interface is of crucial importance and highly relies on the surface preparation quality of the steel element. This paper investigates the influence of steel surface roughness on the mode II fracture toughness and fatigue crack growth behaviour of the bonded composite-to-steel joints. Glass fibre composite and mild structural steel material is considered directly bonded in a wet lay-up process. 4-point end notch flexure (4ENF) tests are conducted on specimens with the steel plates prepared with low, medium and high roughness, respectively. In addition, morphology of the fracture surfaces are characterised by a 3D profilemeter and the friction coefficient is measured by a tribometer for each roughness level. Results show that in quasi-static fracture, fibre bridging is dependent on the surface roughness. A roughness level with $S_q \geq 22$ μm of the steel surface can promote significant fibre bridging thus improved fracture toughness due to enlarged effective bonding area. Under cyclic loading, no fiber bridging is observed across all roughness levels tested. However, the Paris curve parameter C is significantly affected by the roughness level, which decreases by approximately 100 times as the steel surface roughness increases from the low level of $S_q = 5$ μm to high level of $S_q = 22$ μm. The m parameter of the Paris curve remains fairly constant across all the roughness levels tested.

1. Introduction

The composite materials, e.g. fiber-reinforced polymers (FRPs), have been widely used for composites-to-metal hybrid structures in aerospace [1], automotive [2] and construction [3] industry due to its high strength-to-weight ratio, design flexibility, and high fatigue resistance. The synergy of these two materials highly relies on the appropriate joining in between. Among different joining technologies, adhesive bonding is widely utilised due to its effectiveness in load transfer expressed by high stiffness of the connection, exclusion of necessity to drill holes in original steel element, thus no weakening of the original cross-section and faster execution, compared to bolted joint and riveted joint [4]. In the construction field, the bonded joint has been increasingly used in strengthening existing steel structures [5,6] and connecting elements in new structures. Recently an innovative joining technique for steel hollow sections, the wrapped composite joints, was developed by the authors [7,8] to improve the fatigue performance of the traditional welded joints. In this joint, the steel hollow sections are connected

by wrapped glass fibre reinforced polymers (GFRP) through direct bonding at the composite-to-steel interface. No separate adhesive was applied at the interface while the resin of the composite was utilized to provide direct bonding to the steel adherend. While the bonded wrapped composite joints offer significant improvements compared to the welded joints, they still experience debonding failures at the interface when subjected to extreme loading conditions, such as fatigue loading, once the surface of steel is not prepared well enough. Large shear stress concentrations may arise at the end of bonded area due to the contrast in stiffness of the composites and steel materials, thus enhancing the potential of debonding failure. Proper surface preparation of the adherends plays an important role in avoiding such failure in wrapped composite joints. For the composite-to-steel bonded joints, an appropriate preparation of the steel surface should provide sufficient surface roughness that would prevent pure adhesive (interfacial) failure of the bonded connection.

Surface roughness of the metal adherend resulting from different pretreatments has a significant influence on the mechanical properties of the bonded joints. The bonding performance under quasi-static loadings

---

Nomenclature

4ENF	4 point bending end notched flexure
FEA	Finite element analysis
E_1	Young's modulus of the upper arm of the specimen
E_2	Young's modulus of the lower arm of the specimen
h_1	Height of the upper arm of the specimen
h_2	Height of the lower arm of the specimen
B	Width of the specimen
a_0/a	Pre-crack length/crack length
L_a	Lever arm of the specimen
P	Applied force during tests
CSM	Chopped strand mat
$E_{x,t}$	Longitudinal tensile modulus of composites
$E_{y,t}$	Transverse tensile modulus of composites
$E_{x,c}$	Longitudinal compressive modulus of composites
$E_{y,c}$	Transverse compressive modulus of composites
ν_{xy}	In-plane Poisson's ratio of composites
G_{xy}	In-plane shear modulus of composites
E_z	Out-of-plane modulus of composites
G_{xz}/G_{yz}	Out-of-plane shear modulus of composites
ν_{xz}/ν_{yz}	Out-of-plane Poisson's ratio of composites
E	Young's modulus of steel material
f_y	Yield strength of steel material
f_u	Ultimate strength of steel material
S_q	Root mean square roughness
S_{dr}	Developed interfacial area ratio
A	Definition area for roughness measurement
μ	Friction coefficient at the composite-to-steel interface
F_N	Normal force when measuring the friction coefficient
F_x	Horizontal force when measuring the friction coefficient
F_bar_x	Plateau of the horizontal force
CoV	Coefficient of variation
P_{min}	The minimum force during fatigue tests
P_{max}	The maximum force during fatigue tests
R	The force ratio during fatigue tests
DIC	Digital image correlation
SERR	Strain energy release rate
EGM	Extended global method
$G_{II,4ENF}$	Mode II SERR of 4ENF specimen
ψ	Bending stiffness ratio of the upper and lower arm
ξ	Bending stiffness ratio of the upper arm and the whole beam
I_1	Moment of inertia of the upper arm
I_2	Moment of inertia of the lower arm
$(EI)_{eq}$	Equivalent bending stiffness of the specimen
VCCT	Virtual crack closure technique
η	Exponent in B-K criterion of VCCT
P_{crit}	Critical force at crack initiation
G_{Ic}/G_{IIc}	Mode I/II fracture toughness in VCCT
$G_I/G_{II}/G_{III}$	Mode I/II/III SERR in VCCT
G_T	Total SERR in VCCT
$G_{II,ini}$	Initiation value of mode II fracture toughness
G_{eqc}	Equivalent SERR in VCCT
d/d_{ini}	Test displacement /Critical displacement at crack initiation
k	Slope of the crack growth curve after crack initiation
A_1/A_2	The initial and final values of the fracture toughness variation function
x_0	The mid-point of the fracture toughness variation function
p	The power of the fracture toughness variation function
N	Number of cycles during fatigue test
$k_1/k_2/k_3$	Coefficients of the SERR variation surface function
C/C'	Intercept parameter of Paris curves
m	Exponent parameter of Paris curves
q	Intercept parameter of C variation function
b	Exponent parameter of C variation function

has been widely studied during the past decades using metal-to-metal bonded joints. As the primary mechanical property, it is usually characterized by the bond strength or the fracture energy, *G*. Lucchetta et al. [9] investigated the correlation of surface roughness with the adhesion of aluminium sheets in polymer metal hybrid overmolding. They found out that higher surface roughness and glass fibre content lead to a higher shear strength. This is due to the fact that a rough topography helps the polymer to flow within metal surface cavities, and glass fibers anchor the polymer to the substrate. Zhang et al. [10] confirmed by an experimental study that increasing the surface roughness can enhance the fracture toughness of epoxy–aluminium interfaces. Such an enhancement is caused not only by the increase in the actual contact area due to roughness, but also by the change of local mode-mixity, as well as bridging and friction behind the crack. According to van Dam et al. [11], higher surface roughness, S_a, and interfacial area ratios, S_{dr}, result in higher bond strength of steel-epoxy adhesive interfaces. Meanwhile, specimens with similar roughness but altered morphology, which can be reflected by the skewness, S_{sk}, showed further improvement in the adhesion strength. Zhang et al. [12] investigated the surface roughness and bond line thickness on the bonding performance of epoxy adhesive joints on mild steel adherends. It was found out that both bonding strength and elongation at fracture of epoxy adhesive joints improved with the increase of surface roughness of the steel adherends. Smith [13] correlated the mode I and mode II fracture toughness to the surface roughness of a ductile epoxy adhesive bonded to aluminium adherends. It was found out that the mode I fracture energy was influenced by the bond area and is quantitatively correlated to the R_z parameters. The mode II fracture energy was mainly affected by the mechanical

interlocking between the peaks and valleys of the adherends, which is driven by the angle of the hypotenuse of the idealized triangles on the surface, R_z/R_a.

In the case of composite-to-metal bonded structures, additional challenges are imposed to the analysis. The composite member can be laminated directly on the surface of the metallic member as used in the wrapped composite joint [7]. However, existing research has predominantly focused on adhesively bonded joints, where a layer of adhesive or epoxy is applied between the adherends. Hwang et al. [14] conducted the shear lap adhesion test on a composite/steel hybrid joint using a carbon fiber reinforced polymer (CFRP). They found out that the bond strength increased as the surface roughness increased until $R_z = 45$ μm, and decreased at 60 μm. The decrease of the strength at very high roughness levels is related to the fact that the epoxy cannot be uniformly impregnated, and pores are generated at the interface. Arouche et al. [15] showed that inducing a rougher crack propagation path can increase the fracture toughness of CFRP-steel bonded joints. P. Kumar et al. [16] compared the effects of emery-paper roughening and sodium hydroxide treating on the fracture toughness and shear strength of the bonded interface between aluminium alloy skin and FRP patch. The results showed that the latter preparation method led to substantially higher roughness of the surface, thus higher shear strength (44.5 MPa vs. 32.6 MPa) and higher mode II fracture toughness (734.5 J/m^2 vs. 282.4 J/m^2) of the specimen. Manuel A.G. Silva et al. [17] studied the effect of different surface preparations on the bond performance of the CFRP-steel joints by double strap specimens. Pre-treatment with sand blasting and steel gritting improves the surface roughness thus higher shear capacity. J.Ou et al. [18] conducted tests on double lap shear

Table 1

Test specimens.

Loading type	Blasting pressure	Specimens	Total thickness (mm)	Displacement rate / Frequency
Static	low	RL-S-1/2/3	17.64	1 mm/min
	medium	RM-S-1/2/3	17.47	
	high	RH-S-1/2/3	15.38	
Fatigue	low	RL-F-1/2/3	17.64	4 Hz
	medium	RM-F-1/2/3	17.47	
	high	RH-F-1/2/3	15.38	

joints between CFRP sheets and steel, where the steel surface was treated with sand papers of different grit sizes and grit blasting. The results showed the Wenzel roughness factor has a strong positive correlation (with a correlation coefficient of 0.78) with the ultimate load of the joints. Based on the literature review above, it is shown that additional research is required regarding the effects of surface preparation on bi-material structures where a composite member is laminated directly on the surface of a metallic member.

Besides the static behaviour, the influence of surface roughness on the fatigue performance of bonded joints has also been studied by several researchers. Azari et al. [19] investigated the effect of roughness on the steel bonded joints under cyclic loading by double cantilever beam (DCB) and asymmetric double cantilever beam (ADCB) tests. They found out that the fatigue threshold strain energy release rate, G_{th}, increased with the roughness, R_a, until a plateau is reached between 3.9 and 6.4 μm, then decreased for very rough surfaces. Shikimoto et al. [20] investigated the effect of laser patterning pre-treatment on the fatigue strength of adhesive bonded joints using thin steel plates. A significant improvement of the fatigue bond strength was achieved by producing an anchor effect and removing the weak boundary layer. A. Manoli et al.[21] conducted fatigue tests on single lap joints of GFRP plates joined by nanoparticles modified adhesive. Specimens with roughness of R_a= 3.3 μm exhibited an enhancement of 30% of the fatigue life than specimens with R_a= 3.3 μm. Carrera [22] investigated the fatigue life, stiffness degradation and residual static strength of CFRP-to-steel joints with different surface conditions. It was shown that the fatigue life is not affected by the surface characteristic. Specimens with surface pits (high roughness) had a reduction of stiffness degradation under low to moderate fatigue loads compared to specimens with smoother surfaces.

Although the effect of surface roughness on the performance of metal bonded joints has been largely studied using quasi-static tests, the fatigue behaviour has not been thoroughly investigated. Furthermore, existing literature related primarily focused on the total fatigue life of simple joint designs, with limited attention given to study the fatigue crack growth behaviour. Additional research is required on both the static and fatigue fracture behaviour of bi-material bonded joints between metal and composite members.

The present work investigates the influence of surface roughness on the fracture toughness and fatigue crack growth of the composite-to-steel bonded joints, where glass fibre composites are directly bonded to the roughened steel adherends with no separate adhesive layer. Static and fatigue 4-point-bending end notched flexure (4ENF) tests are conducted for specimens with different surface roughness. The roughness of the steel plate and the fracture interface is characterised by a 3D profilemeter. The friction coefficients between the fractured interface are measured by a tribometer, serving as the inputs for interpretation strain energy release rates (SERR) through finite element models which take the friction effect into account. The surface roughness is correlated with the fracture toughness and fatigue resistance in the end.

2. Specimens and surface characterisation

2.1. Specimens and materials

In this study, a total of 18 bonded joint specimens are used for the static and fatigue 4ENF tests as shown in Table 1. For each loading type, surface of the mild S275 steel plates were grit blasted with low, medium and high blasting pressures, respectively, to achieve 3 different surface roughness. 3 identical specimens were tested for each configuration. The steel-composite specimens were manufactured by hand lay-up of the glass fiber plies on the steel treated surface. Before lamination, the surfaces of steel plates were chemically degreased to ensure good bonding quality and a non-adhesive insert of 32 μm thickness was placed to induce a pre-crack between steel and composite arms. Each composite ply is formed by woven glass fibre reinforcement fabric interleaved with chopped strand mat (CSM) and a vinyl ester matrix system with fibre volume fraction of approximately 30%. CSM layer is adjacent to the steel-composite interface. Finally, steel-composite specimens are cut from the plates using water jet. Geometry and dimensions of the specimens used in this study are shown in Fig. 1. The half-span (L), width (B), upper and lower arm thicknesses (h_1 and h_2), pre-crack length (a_0) and the load-to-support point distance (L_a) are indicated in the figure. For the bi-material configuration, the thicknesses of steel and composites are designed to meet the criterion described in Eq. (1), such that the two arms have the same longitudinal strain at the faying surfaces to obtain a pure mode II loading condition [23].

$$E_1 h_1^2 = E_2 h_2^2 \tag{1}$$

where E_1 and E_2 are the elastic modulus in the longitudinal direction for the upper and lower arms, respectively. The actual thickness of the specimens vary among different roughness series due to variation of applied pressure during hand lamination and curing conditions. The measured average total thickness of the specimens are listed in Table 1.

The material properties of steel plates and composite laminate are obtained by standard tensile/compressive coupon tests according to ISO [24–27] and are summarised in Table 2.

2.2. Surface roughness

The surface roughnesses of the steel plates were measured by a 3D optical profilemeter (Keyence VR6000) with 40 × magnification. The surface roughness was obtained from two 20 × 20 mm areas selected on the steel plates of each roughness series. Optical images and 3D profiles of the scanned areas for each roughness series are shown in Fig. 2. It can be seen that, compared to the relatively smoother surface of low roughness, sharper peaks and valleys are found in the medium and high roughness plates. Two surface roughness parameters, namely S_q and S_{dr}, are chosen here according to [28] with the definition given by Eqs. (2) and (3). S_q represents the root mean square value of ordinate values within the definition area, A. It is equivalent to the standard deviation of heights. Since different surface profiles can have similar S_q values, another parameter, the developed interfacial area ratio S_{dr}, is selected to assess the surface topology. S_{dr} is expressed as the percentage of the definition area's additional surface area contributed by the texture as
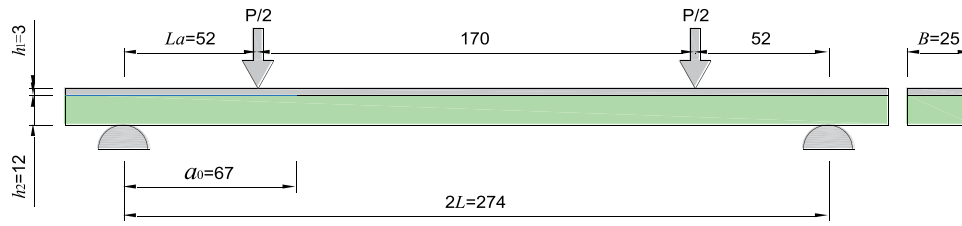
Fig. 1. Dimensions of specimen (in millimetres).

Table 2
Materials properties.

Material	Mechanical property	Average value and (CoV [%])
Composites	Longitudinal and transverse compressive modulus – $E_{x,c} = E_{y,c*}$	12077.11 MPa (4.50)
	Longitudinal and transverse tensile modulus – $E_{x,t} = E_{y,t}*$	11798.20 MPa (6.37)
	In-plane Poisson's ratio – ν_{xy}	0.15 (6.50)
	In-plane shear modulus – G_{xy}	3120 MPa (6.81)
Steel	Young's modules – $E**$	190 MPa (5.42)
	Yield strength – f_y	278.30 MPa (0.22)
	Ultimate strength – f_u	637.83 MPa (0.40)

*E_2 equals to the average of the compressive and tensile modulus in the present study
**equals to E_1 in the present study

compared to the planar definition area. The average measured results for each roughness series are summarised in Table 3. From low to high roughness, the S_q value increases from 4.56 to 21.99 μm, while the developed interfacial area ratio S_{dr} increases from 0.99% to 11.67%. S_{dr} is plotted against S_q in Fig. 3 and a quiet linear relationship can be found between these two parameters, indicating that a rougher surface leads to a larger developed interfacial area.

$$S_q = \sqrt{\frac{1}{A}\iint_A Z^2(x,y)\,dxdy} \tag{2}$$

$$S_{dr} = \frac{1}{A}\left[\iint_A \left(\sqrt{\left[1+\left(\frac{\partial z(x,y)}{\partial x}\right)^2+\left(\frac{\partial z(x,y)}{\partial y}\right)^2\right]}-1\right)dxdy\right] \tag{3}$$

Table 3
Surface roughness measurement results.

Parameters	S_q (μm)	S_{dr} (%)
Low roughness	4.56 ± 0.75	0.99 ± 0.16
Medium roughness	14.14 ± 1.24	5.87 ± 0.06
High roughness	21.99 ± 0.62	11.67 ± 0.46

Table 4
Fracture toughness.

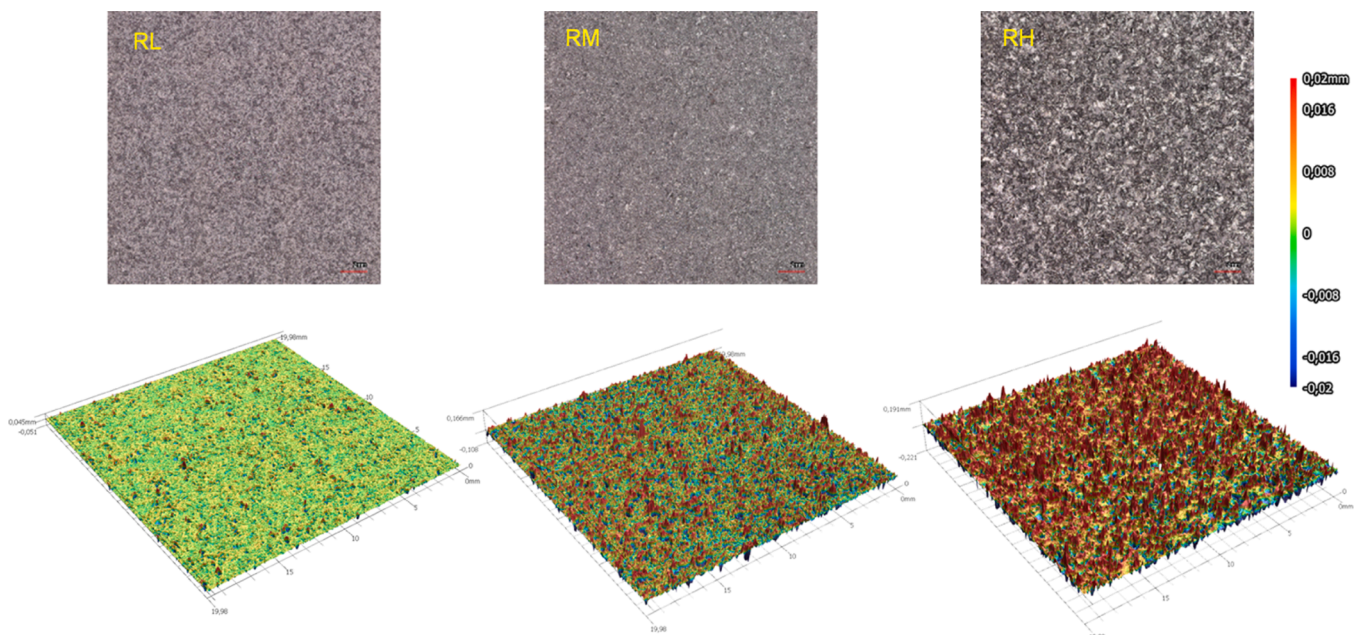| Specimens	$P_{crit,test}$ (kN)	$P_{crit,FEA}$ (kN)	Error (%)	$G_{II,ini}$ – EGM (N/mm)	$G_{II,ini}$ – VCCT (N/mm)
RL-S-1	2.05	-	-	0.49	0.39
RL-S-2	2.09			0.50	0.40
RL-S-3	3.10			1.11	0.85
Average	2.41	2.43	0.77	0.70	0.55
RM-S-1	5.74	-	-	3.82	2.27
RM-S-2	5.47			3.47	2.06
RM-S-3	4.68			2.54	1.86
Average	5.30	4.87	-8.07	3.27	2.07
RH-S-1	4.40	-	-	3.33	2.15
RH-S-2	4.96			4.24	2.61
RH-S-3	4.84			4.03	3.70
Average	4.73	5.00	-5.61	3.86	2.82

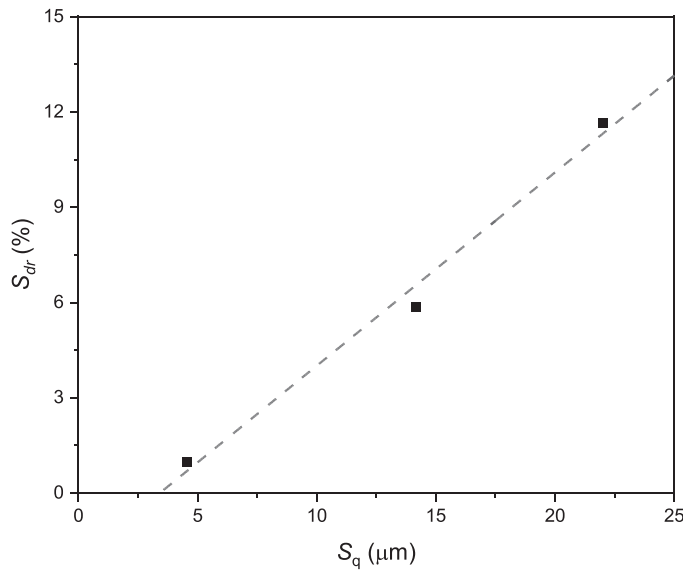**Fig. 2.** Optical image and 3D profile of steel surface with different roughness.

Fig. 3. Relationship between S_q and S_{dr}.

2.3. Friction coefficient

In order to account for the friction effect between the cracked surfaces in fracture and fatigue crack growth tests, the friction coefficients were measured at the pre-crack region and the fractured composite-to-steel interface after the tests. Fig. 4 shows the samples cut from the fractured specimens in static tests, whose failure modes will be discussed in detail in Section 4.1. Three samples are cut from the pre-crack region, with the insert remaining on top of the composites. Nine samples are cut from the fractured interface, with three samples selected from each roughness series. The friction coefficient was measured by a multi-function tribometer (Rtec MFT-5000). As shown in Fig. 5(a), the normal force, F_N, is applied on the steel plate through a customized cylinder. The composite laminate is fixed on the bottom and moves with the XY stage. A load cell embedded in the horizontal direction is used to monitor the friction force, F_x. During the fatigue 4ENF test, an obvious relative movement is observed between the fractured steel and composite arms. Therefore, a relatively large amplitude, i.e. 0.8 mm, is chosen here to mimic the reciprocating gross slip regime during the test. The composite laminate moves in the X direction, leading to the same relative movement direction against the steel arm during the 4ENF tests. Samples cut from fatigue tested specimen are measured with 4 Hz, which is the same as that used in the fatigue tests, while samples cut from the static tested specimen are measured with 0.2 Hz to mimic the quasi-static process.

A typical frictional hysteresis loop is shown as Fig. 5(b). The friction force remains nearly constant around the middle position but increases obviously at the extreme position. This results from the decreasing velocity when the movement direction changes and the static friction, instead of kinetic friction, takes place. Since the influence of friction on the SERR at the crack tip is related to energy dissipation mechanism during the kinetic friction process, the average friction force at the plateau (red dash line in the figure), $\overline{F}_x$, is employed to calculate the friction coefficient by the equation of $\mu = F_N/F_x$. The friction coefficient variation against number of cycles is shown in Fig. 5(c), where each point in this figure represents average results of two directions. The plateau of the curve is taken as the result of each sample to exclude the possible 'running-in' effect [29] during the initial cycles. Average friction coefficients between the cracked surfaces of the different roughness under fatigue (4 Hz) and quasi-static (0.2 Hz) loading protocols are shown in Fig. 5(d). The friction coefficient increases slightly with the surface roughness for both cases. Specifically, friction coefficient at 4 Hz increases by 10.9% from 0.46 for low roughness series to 0.51 for high roughness, while friction coefficient at 0.2 Hz increases by 9.6% from 0.52 to 0.57. Friction coefficient at 0.2 Hz are 12% to 19% higher than those at 4 Hz for different roughness. It should be noted that the results of all the samples reflect friction coefficients at the fractured surfaces, instead of the pure interface between steel and composite materials. The failure modes will be further discussed in the following sections. In addition, the friction coefficients at the pre-crack region are 0.23 under 4 Hz and 0.3 under 0.2 Hz. This values are relatively lower than that in the fractured interfaces due to the existence of an insert between the surfaces. The measured friction coefficients will be used in the FE models
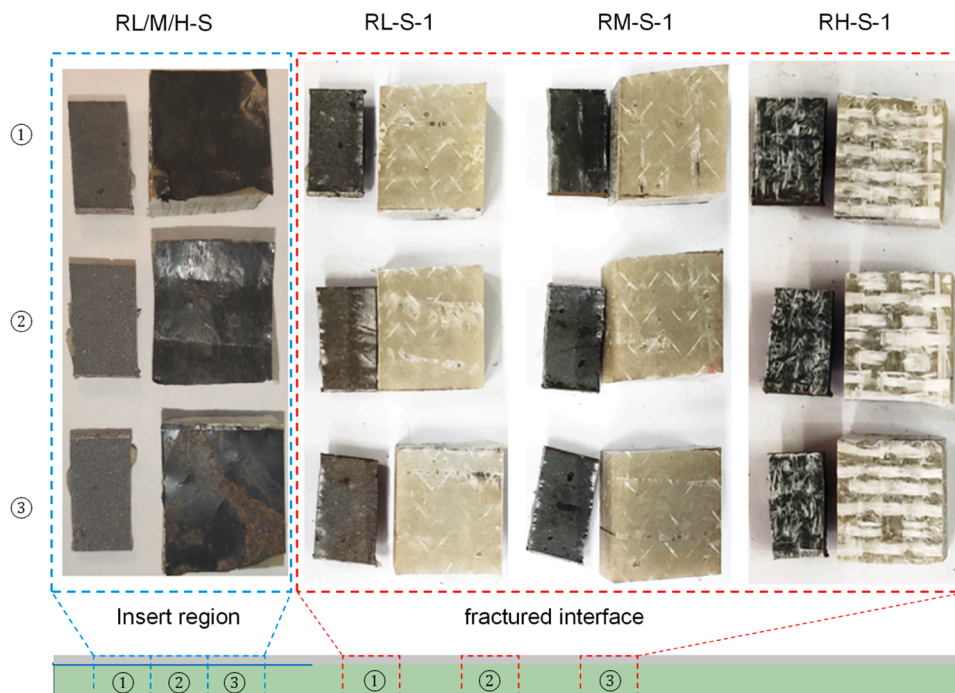

Fig. 4. Samples used for measuring friction coefficient (from static tested specimens).
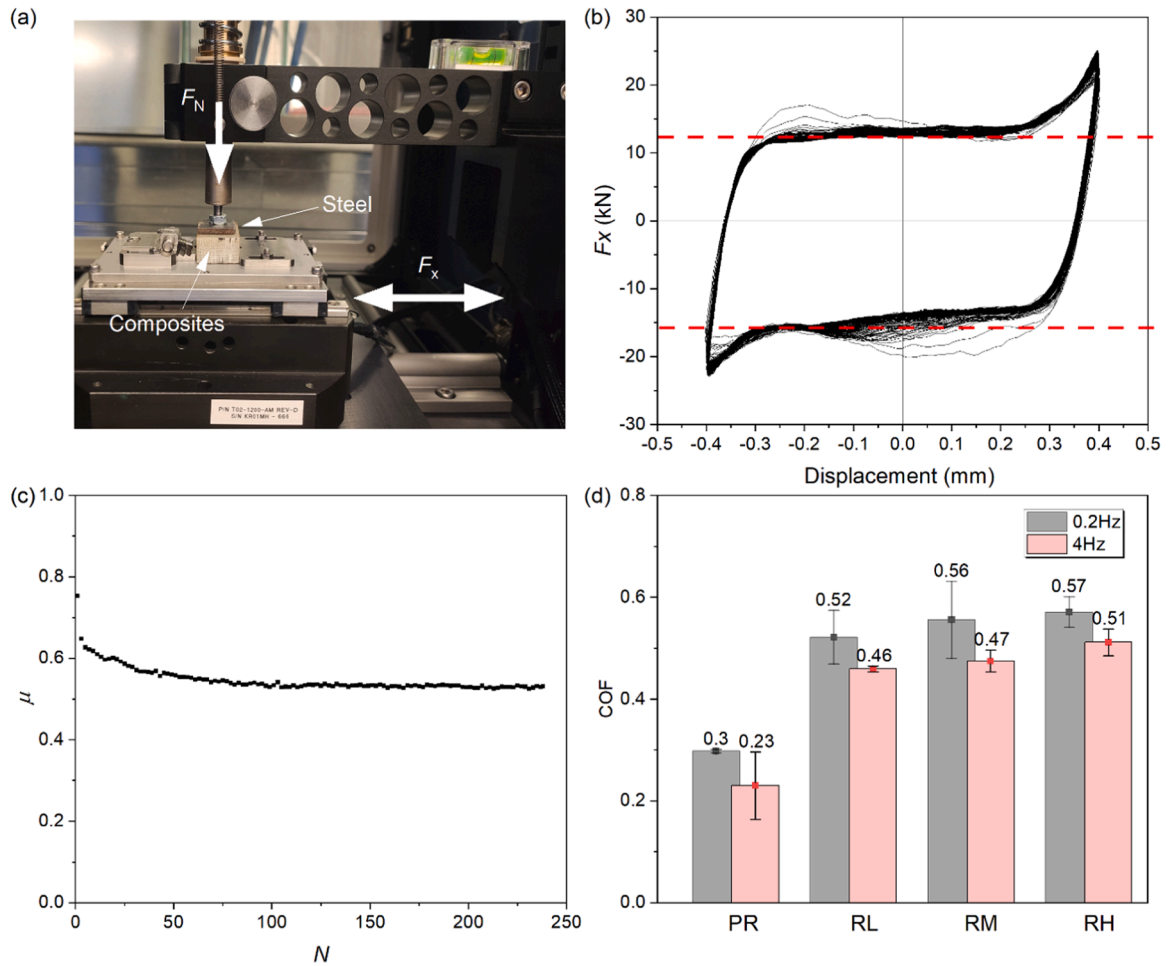
Fig. 5. Friction coefficient measurement: (a) test set-up; (b) frictional hysteresis loops; (c) friction coefficient versus cycles; (d) friction coefficient versus surface roughness.

for each roughness series under both static and fatigue cases in the later sections.

3. Experimental methods

3.1. Test set-up, instrumentation and loading protocol

Tests were conducted in a universal testing machine (UTM) with a load cell of 15 kN. The 4-point bending test set-up is shown in Fig. 6, where the steel arm is on top to avoid crack migration to the composite layers [30]. The specimens are loaded by two loading cylinders attached to a loading beam, which is connected to the actuator by a shaft such that equal forces are applied on the two loading points. The static tests are conducted by displacement control with the loading rate of 1 mm/min, while the fatigue tests are conducted by displacement control with the frequency of 4 Hz. For the fatigue tests, the load ratio $R = 0.1$, namely $P_{min}/P_{max} = 0.1$, is adopted. For each roughness series, the fatigue tests are started with the force level (P_{max}) corresponding to 60% of the critical SERR obtained by the static tests. This starting load level is chosen to be high enough to cover as wide SERR range as possible since the SERR values will decrease during the tests, but to be low enough to avoid too fast crack propagation (e.g. 0.1 mm/cycle) for the convenience of crack length monitoring.

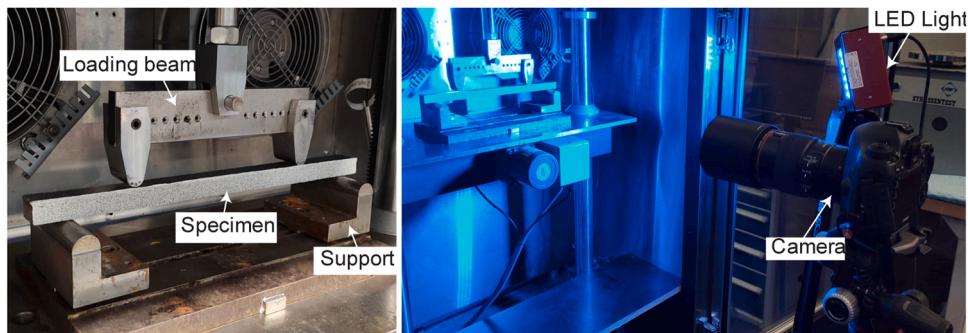A white paint coating followed by a black speckle pattern is applied

Fig. 6. Test set-up and instrumentation.

on one side of the specimens to allow measurements by digital image correlation (DIC). The speckle size is chosen between 0.2 and 0.5 mm based on the requirement of DIC analysis. A digital camera (51 Mpx) assisted by a LED light is positioned perpendicularly to the specimen for crack length monitoring during the tests. With the camera connected to the controlling system, photos are taken at the minimum and maximum displacements every 500 cycles or every 1% stiffness degradation. Shear strains are extracted at the interface afterwards during the DIC analysis and are quantified by the strain thresholds to determine the crack length. The explanation of crack monitoring technique can be found in [31].

3.2. Fracture data analysis

The crack growth driving force is calculated by the extended global method (EGM), proposed by Moslem, et al. [32] based on the global method by Williams [33]. The global method is developed based on the beam theory where the SERR is calculated by the bending moments and loads in a cracked specimen. EGM modified this global method in order to consider asymmetric cases where the crack propagates between two different orthotropic layers. The mode II SERR at the crack tip of 4ENF specimens can be calculated as:

$$G_{II,4ENF} = \frac{P^2 L_a^2}{8BE_1I_1}\left(\frac{1}{1+\psi} - \xi\right)$$ (4)

where ψ and ξ are the bending stiffness ratios of arms for the specimens, which can be calculated by:

$$\psi = \frac{E_2 I_2}{E_1 I_1}$$ (5)

$$\xi = \frac{E_1 I_1}{(EI)_{eq}}$$ (6)

In **Eq.** (4), (5) and (6), E_1 and E_2 are the longitudinal modulus of the upper and lower arms. I_1 and I_2 are the moment of inertia of the upper lower arms, respectively. $(EI)_{eq}$ is the equivalent bending stiffness of the specimen.

Another commonly used method for calculating SERR at the crack tip is the virtual crack closure technique (VCCT), based on finite element (FE) model. The VCCT assumes the energy released for a small crack extension is equal to the work required to close the crack to its original length. By the VCCT, all components of the SERR can be obtained while the influence of friction on the SERR values at the crack tip is taken into account [31]. A 3D finite element analysis (FEA) is performed in ABAQUS software. The geometry and boundary conditions of the FE model follow the design of the 4ENF specimens, as shown in Fig. 7. The specimen dimensions are taken as the average measured values indicated in

Table 1. Elastic and plastic material properties, indicated in Table 2, are defined for the steel arm. The composite laminate is modelled as one piece of solid part in this model. As stresses in the composite during the tests are much lower than the strength of the material, only elastic material properties are used to model the composite laminate. Transversely anisotropic material properties are defined based on the tests results shown in Table 2 for the in-plane properties of the laminate: E_x, E_y, G_{xy} and v_{xy}. In absence of experimental data, the out-of-plane elastic properties of the laminate E_z, $G_{xz}=G_{yz}$, $v_{xz}= v_{yz}$ were estimated through the classical laminate theory for an equivalent unidirectional material. Linear, hexahedron 8–noded solid elements with reduced integration (C3D8R) are used for both steel and composite parts.

The VCCT fracture criterion in combination with a friction behaviour are defined for the composite-to-steel interface. When modelling the fracture behaviour, the Benzeggagh–Kenane mixed-mode criterion is employed as Eq. (7):

$$G_{eqc} = G_{Ic} + \left(G_{IIc} - G_{Ic}\right)\left(\frac{G_{II} + G_{III}}{G_T}\right)^{\eta}$$ (7)

where G_{eqc} is the equivalent critical SERR, G_{Ic} and G_{IIc} are the critical mode I and mode II SERRs, $G_T =G_I+G_{II}+G_{III}$, and $\eta = 1.8$. Since mode I is not relevant in this study, the same critical value is defined for the mode I and mode II SERRs. While the FE model is used to obtain SERRs at a stationary crack tip, sufficiently high instead values of critical SERRs, e. g. 100 N/mm, rather than the actual values, are provided in the analysis to prevent crack propagation. The penalty friction formulation is defined for the tangential behaviour. The friction coefficient of 0.3 and 0.23 are used for the pre-crack region and in the range of 0.46–0.57 for the fractured interface of different roughness series in the static and fatigue test models based on measurements presented in Fig. 5(d). To account for the friction effect at the contact area between the loading/supporting cylinder and the specimen, a commonly used friction coefficient, 0.3, is also defined in these interactions. A mesh sensitivity study has been discussed in [31] and a global mesh size of 1 mm with aspect ratio of 1 is used considering the convergence of SERR values and computing efficiency. A typical SERR distribution at the crack tip (with a=67 mm, $P = 2$ kN) is shown in Fig. 8. Unrealistic values at the edges resulting from algorithm problems are excluded. It is shown that mode II component dominates the whole crack width except for the edges, where mode III arises due to transverse shear deformation of the composite. This proves that the strain-based design for the thickness of the specimen according to Eq. (1) can successfully guarantee the pure mode II behaviour and the variation of the thickness due to manufacture does not affect the results. The average mode II SERRs at the plateau are considered for the analysis.
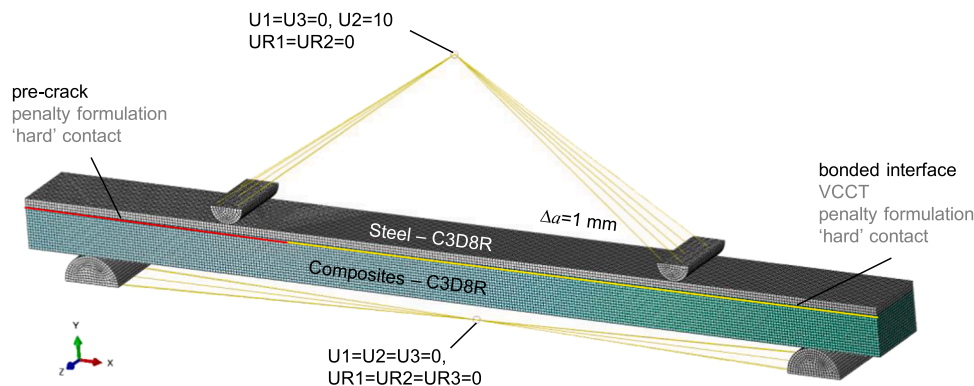

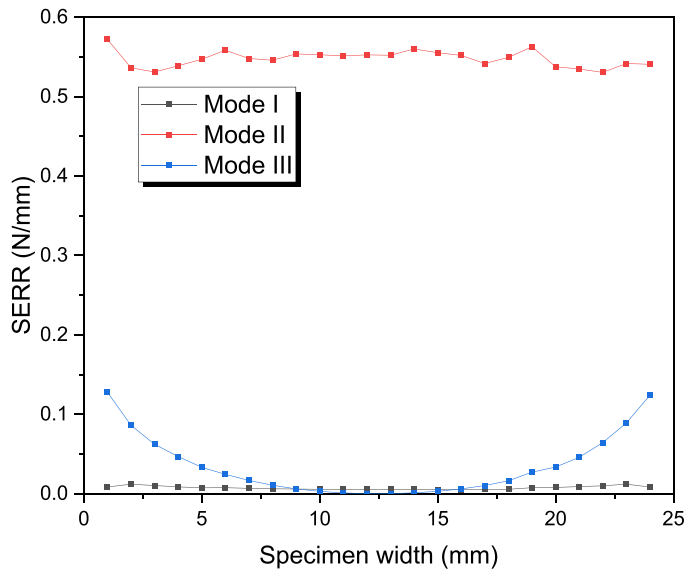
Fig. 7. Mesh topology and boundary conditions of FE model.

Fig. 8. SERR components and distribution along specimen width (a=67 mm, P = 2 kN).

4. Static test results

4.1. Failure modes

The full field shear strain is analysed using DIC. Deformations of a representative specimen (RH-S-1) is shown in Fig. 9 at three different stages during the static test. Shear strains along the interface increases once debonding happens. The crack length can be determined based on the strain threshold as explained in Ref. [31] It is observed that the crack develops along the composite-to-steel interface towards the right loading point as the force increases.

After the static tests, specimens are opened along the fracture interface for observation of the failure modes and fracture surface morphology. Fig. 10 shows representative fracture surfaces of specimens from each roughness series, including both optical images and 3D height profiles. Limited amount of resin remains attached covering less than 5% of the steel surfaces, for low and medium roughness series, and no laminate tearing is found on the composite surfaces. This indicates a dominant adhesive failure at the interface. For low and medium roughness series, the strength of the composite-to-steel interface bonding is lower than that between cthe omposite layers. For the high roughness series, however, resin and chopped strands covers almost entirely the steel surface along the fracture plane, except for the areas near the pre-crack. The crack initiated at the interface but immediately migrated into the adjacent CSM layer of the composite material. For this series, the steel surface roughness provided enough bond strength at the composite-to-steel interface allowing to engage the crack propagation with fibre tear through CSM and between CSM and woven fabric which provides more fracture toughness.

4.2. Force-displacement response

Force-displacement-crack length responses of all the specimens are shown in Fig. 11. The displacements were extracted from DIC using the average vertical displacements of the facet points 1 and 2 created on the specimen under the loading points, as shown in Fig. 9, minus the average vertical displacements of the faced points 3 and 4, created on the specimen next to the support points. This excludes non-linearities of the loading fixture. The crack length is monitored by 2D DIC, analysed by the normalized shear strain method, introduced in [31]. The cack length a is measured as distance from the left support point to the crack front, as indicated in Fig. 9. The initial crack length is approximately a_0 = 52 mm, varying 2–3 mm between the specimens which is taken into account in the further analysis in calculating crack extensions. The initial crack lengths and their development for all specimens are shown in secondary axis of in Fig. 11. As can be seen in Fig. 11 (a) and (b), for low and medium roughness series, the force-displacement curves remain linear until reaching the peak (critical) load level, after which a sudden drop of the force is observed. Correspondingly, cracks of the specimens propagated immediately once they initiated at the peak loads, indicating that the unstable crack growth is mainly due to adhesive failure. Specifically, for two of the low roughness specimens the cracks propagate instantly to 100–130 mm and gradually until 200 mm near the right loading point, while for the remaining one the crack fully propagates to the 200 mm immediately. For the medium roughness specimens the cracks propagate instantly to 140 – 180 mm and stabilized after that. The initial stiffness varies among different specimens due to small variations of specimen thickness and initial crack length. The critical loads
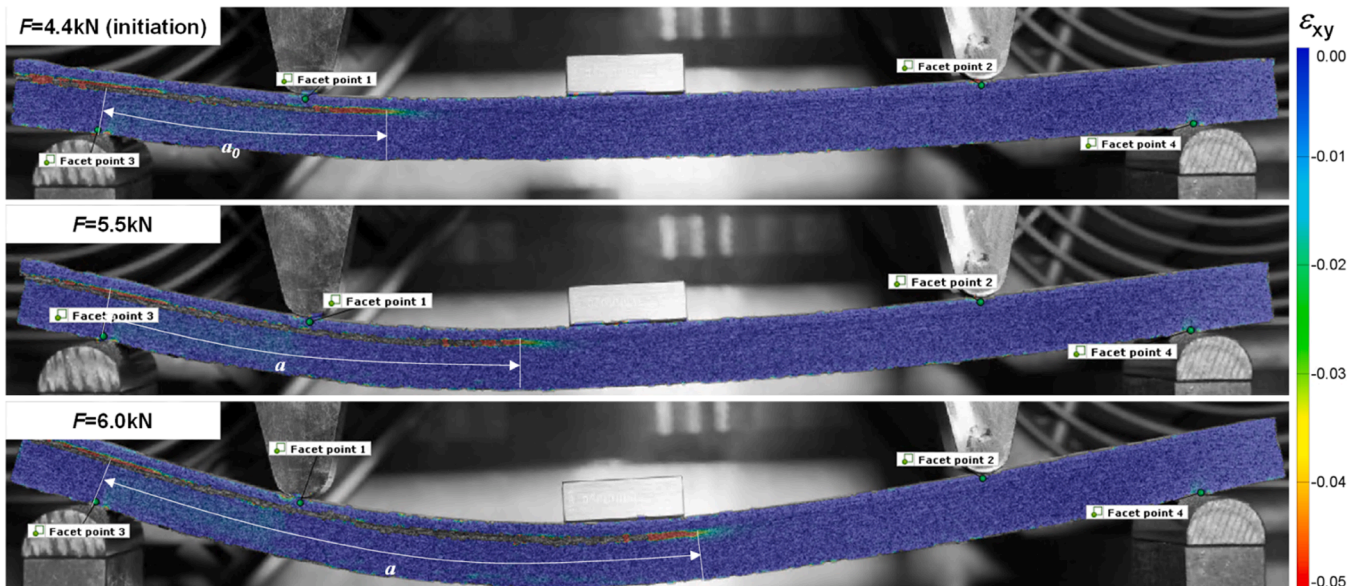

Fig. 9. Representative strain field and crack propagation at three different stages (specimen RH-S-1).
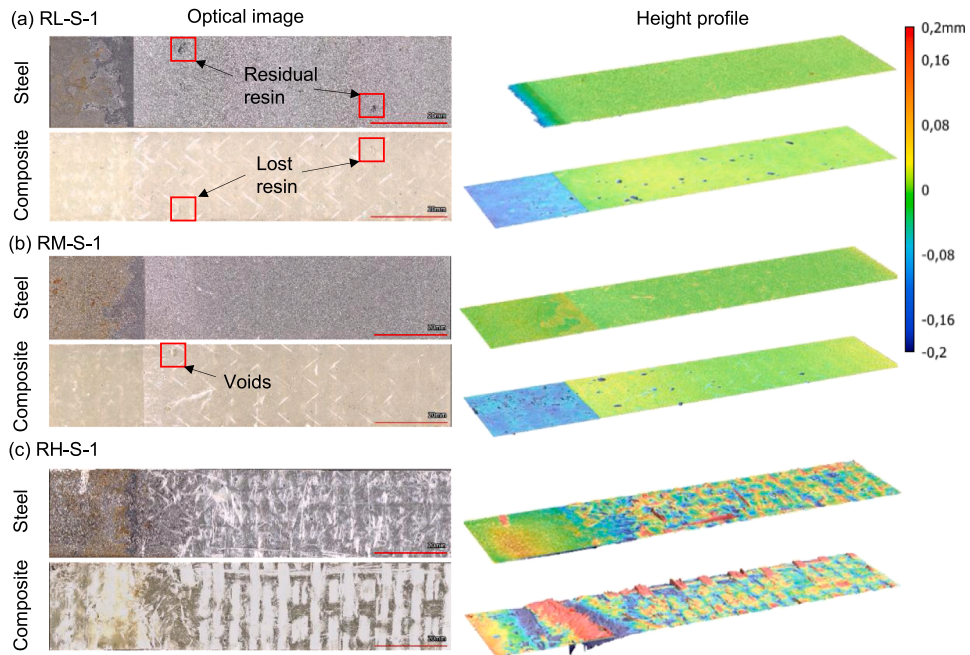
Fig. 10. Representative fracture surfaces of static tested specimens.
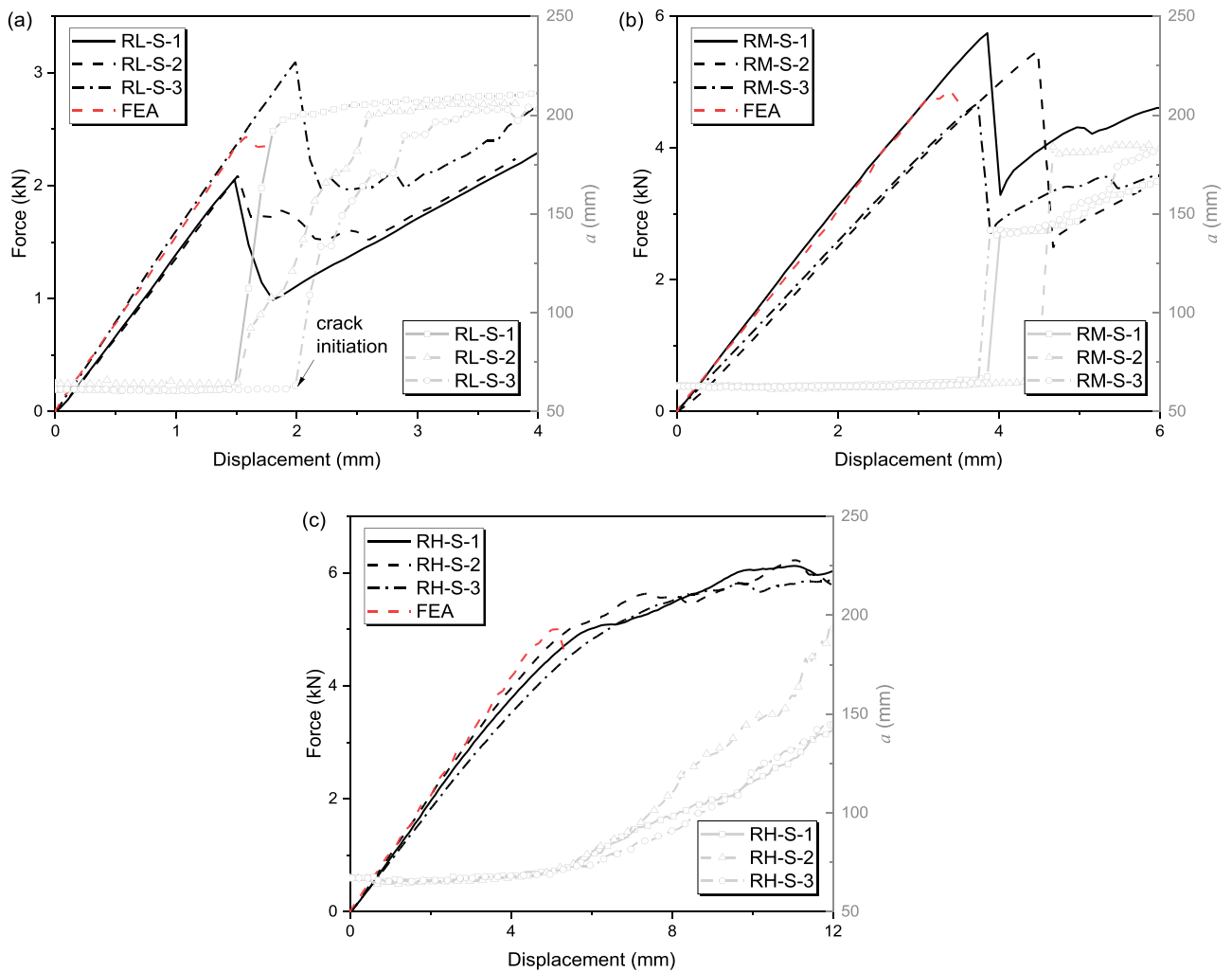

Fig. 11. Static force-displacement response and crack development of (a) RL series, (b) RM series and (c) RH series.

are between 2 and 3 kN for the low roughness series and from 4.7 to 5.7 kN for the medium roughness series. High roughness series shows comparable critical loads to the medium roughness series. However, the force of high roughness specimens keeps increasing after crack initiation, at around 4.4 kN, until reaching 6.5 kN at end of the tests. In these specimens, cracks grow gradually after initiation.

Since no sudden force drop is observed in the force-displacement curves for the high roughness series, and the non-linearity of force-displacement curves may reflect not only crack development but also plasticity in the steel arm, the crack initiation for the high roughness series was determined based on the crack growth curves, as the one shown in Fig. 12, instead of the force variation. To detect the crack initiation point, crack length-displacement curves are fitted with a piecewise function [34]:

$$a = f(d) = \begin{cases} a_0, & d \leq d_{ini} \\ k(d - d_{ini}) + a_0, & d > d_{ini} \end{cases} \quad (8)$$

where a_0 is the pre-crack length, d is the test displacement and k is the slope of the crack growth curve after crack initiation. The crack length remains constant, as a_0, until the displacement at crack initiation, d_{ini}. After initiation, the crack length measurements are fitted using a linear function. The values of fitting parameters a_0, k and d_{ini} are determined by the least squares method. The fitted results of d_{ini} values for the three specimens are 4.84, 5.38 and 6.05 mm, respectively. The initiation values of SERR for these specimens are calculated based on the corresponding critical loads.

4.3. Fracture toughness

The initiation value of the mode II SERR, $G_{II,ini}$, was calculated by substituting the critical loads into Eq. (4) of the EGM. The SERRs are also extracted at the same load levels from FE models with the friction coefficient defined at the interface. The initiation SERR values obtained from the EGM and VCCT are summarised in Table 5. The average initiation SERR obtained from the VCCT for each roughness series serve as the critical SERR to model the fracture behaviour, as in Eq. (7). Force-displacement curves were extracted from the model and plotted together with the experimental results in Fig. 11. Due to the limitation of the VCCT in terms of simulating ductile crack behaviour, the numerical results are only exhibited until the sudden force drop. The initial stiffness matches well with experimental results and the predicted critical loads are within 10% range of the test results, as shown in Table 5.
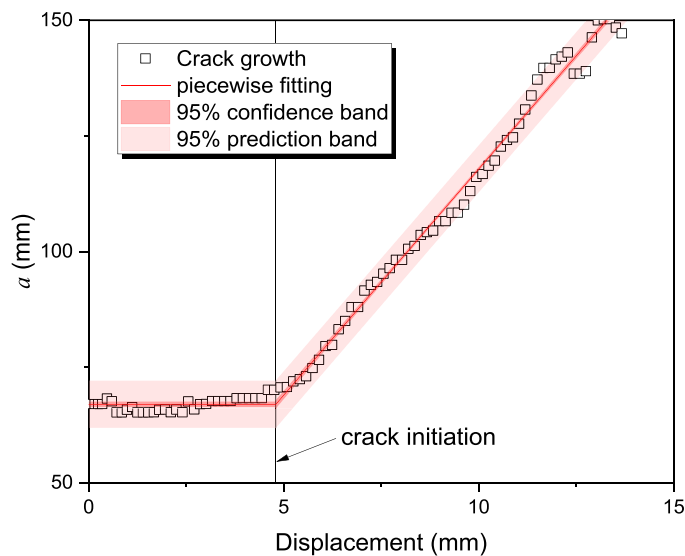
Fig. 12. Determination of crack initiation by pricewise fitting on crack growth curve (example specimen RH-S-1).

Table 5
Fitted results for SERR vs. force and crack length.

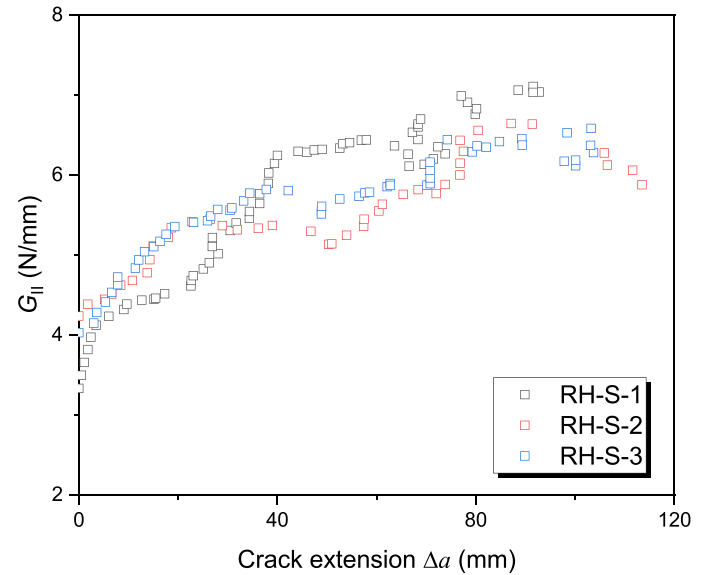| Coefficients			R^2		
RL	RM	RH	RL	RM	RH
$k_1 = 0.084$, $k_2 = -2.14\text{E-5}$, $k_3 = 0.0038$	$k_1 = 0.084$, $k_2 = -1.30\text{E-4}$, $k_3 = 0.029$	$k_1 = 0.12$, $k_2 = 2.23\text{E-4}$, $k_3 = 0.019$	0.99	0.98	0.98

Fig. 13. Mode II SERR versus crack extension for RH specimens.

Since specimens from low and medium roughness series experienced unstable crack propagation, the resistance curves (R-curves) were only obtained for the high roughness series, as shown in Fig. 13. The SERR increases from 3.8 N/mm corresponding to the initiation value, to a plateau, up to and above 6 N/mm, as the crack propagates. Such high value of SERR corresponding to crack propagation is attributed to fibre bridging, identified in profile images in Fig. 10 (c).

The initiation values of SERR are plotted against the surface roughness parameters S_q and S_{dr}, as shown in Fig. 14. It is found out that calculated based on EGM, the average $G_{II,ini}$ increases dramatically by 367%, from 0.7 N/mm to 3.27 N/mm, as the roughness transitions from low to medium level, while increases by only 18%, from 3.27 N/mm to 3.86 N/mm, as the roughness shifts from medium to high level. The same variation trend is also found in results based on VCCT, where $G_{II,ini}$ increases dramatically by 276%, from 0.55 N/mm to 2.07 N/mm, but only by 36%, from 2.07 N/mm to 2.82 N/mm for roughness transition from low to medium, and from medium to high levels, respectively. In addition, the $G_{II,ini}$ calculated from the EGM is 27% higher than the value calculated from VCCT for the low roughness, and over 58% and 35% higher for medium and high roughness series, respectively. This difference is mainly from the energy dissipated by the friction effect at the cracked surface underneath the loading point, as well as the contact area between the loading/support cylinder and the specimen [31], which cannot be excluded in EGM. Higher roughness corresponds to higher loading forces therefore lager frictional forces, thus resulting in a larger influence between the SERR values based on FEA and EGM.

Literature [9,14,16] shows that the improvement of fracture toughness with the surface roughness is related to the increased effective bonding area. This is also the case in the current study from the relationship between $G_{II,ini}$ and S_{dr} in Fig. 14 (b). However, the $G_{II,ini}$ doesn't increase linearly with S_{dr} and tends to be a steady value at high roughness levels. This may be because that the effect of roughness diminishes when the fracture path moves away from the interface [19].
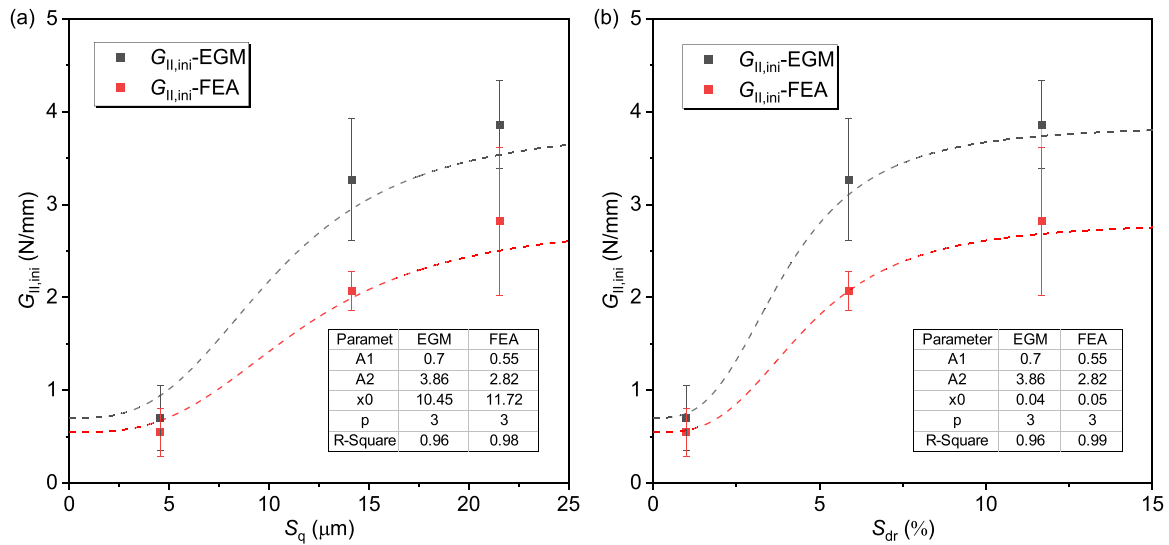
Paramet	EGM	FEA
A1	0.7	0.55
A2	3.86	2.82
x0	10.45	11.72
p	3	3
R-Square	0.96	0.98

Parameter	EGM	FEA
A1	0.7	0.55
A2	3.86	2.82
x0	0.04	0.05
p	3	3
R-Square	0.96	0.99

Fig. 14. Correlation between mode II SERR and surface roughness using (a) S_q and (b) S_{dr} parameters.
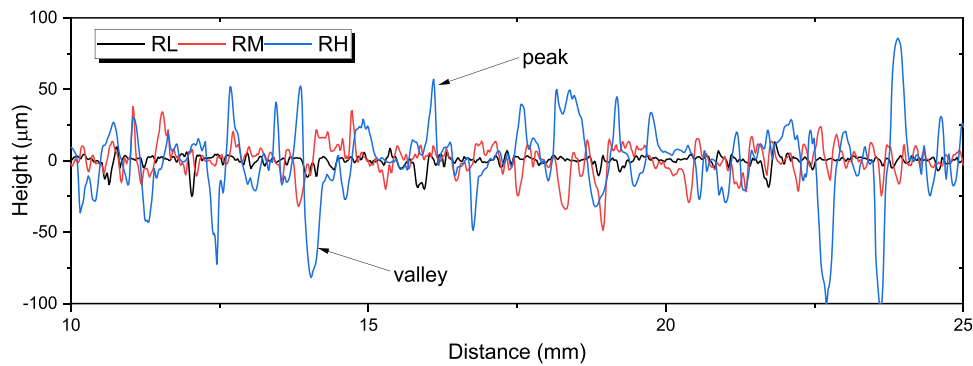

Fig. 15. Height profiles of steel surfaces with low (RL), medium (RM) and high (RH) roughness.

Other mechanisms may also be responsible for the variation trend of the fracture energy measured from the tests. The highly irregular surface, as shown in Fig. 2(c), and height profile, shown in Fig. 15, of high roughness series enable the resin of the composites to deeply penetrate into the steel surface, thus enlarging the effective bonded area and enhancing the mechanical interlocking between these two adherends. The presence of fibre bridging, observed in Fig. 10 (c), significantly contributes to the increased fracture toughness as well. Overall, a larger effective bonding surface, mechanical interlocking, and fibre bridging are the major factors that contribute to the increase of fracture toughness. In addition, literature [14,19] indicates that the bond performance will deteriorate after reaching a certain roughness level. A typical explanation [19] is that the increase of roughness reduces the wettability of the substrate such that the adhesive cannot properly spread on the steel surface and contribute to the formation of air voids during production. Meanwhile, it is reported in [19] that, above a certain roughness level, the stress concentration at the tip of asperities may reduce the strength of the adhesive joints. It is the combination of all the mechanisms mentioned above that contribute to the unique trend of $G_{II,ini}$ versus roughness levels.

Considering the decreasing rate of the increase of SERR values as the roughness parameters increases, a logistic regression in ORIGIN software is applied for characterising the relationship between the two as defined in Eq. (9). SERR is chosen as dependent and roughness as independent variable.

$$y = \frac{A_1 - A_2}{1 + (x/x_0)^p} + A_2 \tag{9}$$

where A_1, A_2 are the initial and final values of the depended variable, x_0 is the mid-point and p is the power of this function. The parameters in this equation is fitted by the least squares method and the results are listed in the table of Fig. 14.

5. Fatigue test results

5.1. Failure modes

A typical shear strain field of a representative specimen (RH-F-1) is shown in Fig. 16 at different number of cycles during the fatigue test at the state of maximum load. The crack is indicated by the region of high shear strains at the interface and the same method is applied to determine the crack length as in Fig. 9, following the DIC facilitated crack length determination procedure that is detailed in [31]. The crack grows from the pre-crack location towards the right loading point in a stable manner. Position of the crack is maintained at the interface between steel and composite.

After the cyclic tests, specimens were opened along the fracture interface for inspection. Optical images and height profiles of a representative specimen from each roughness series are shown in Fig. 17. It is found that the predominate failure mode for the low and medium roughness series is adhesive failure at the composite-to-steel interface. The fracture surfaces are smooth with only small portions of resin
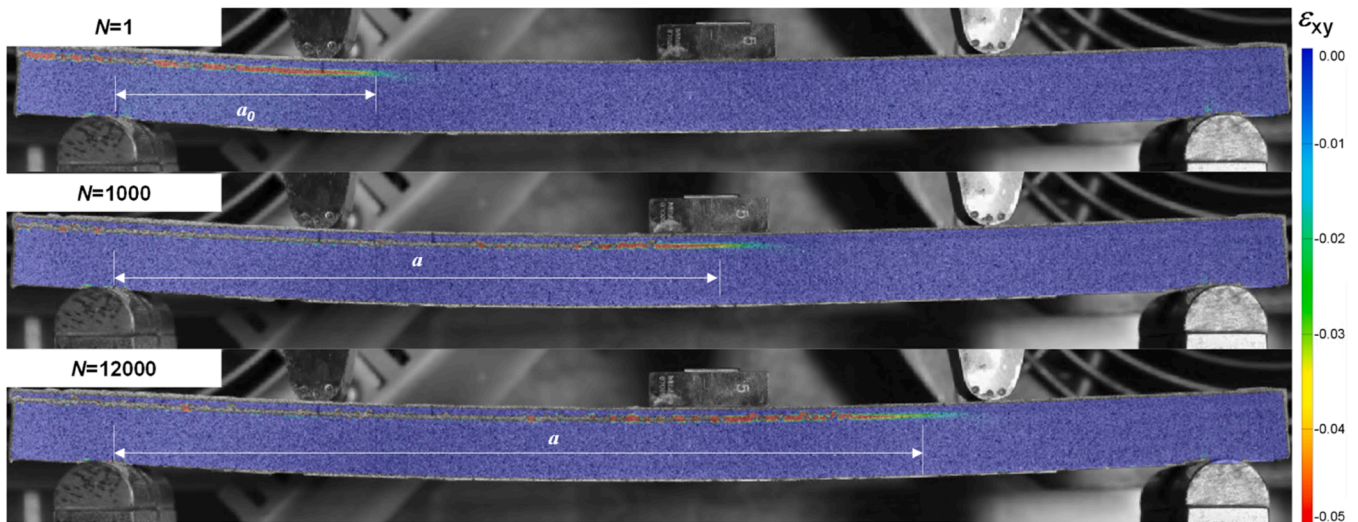
Fig. 16. Representative strain field and crack propagation at three different stages (specimen RH-F-1).
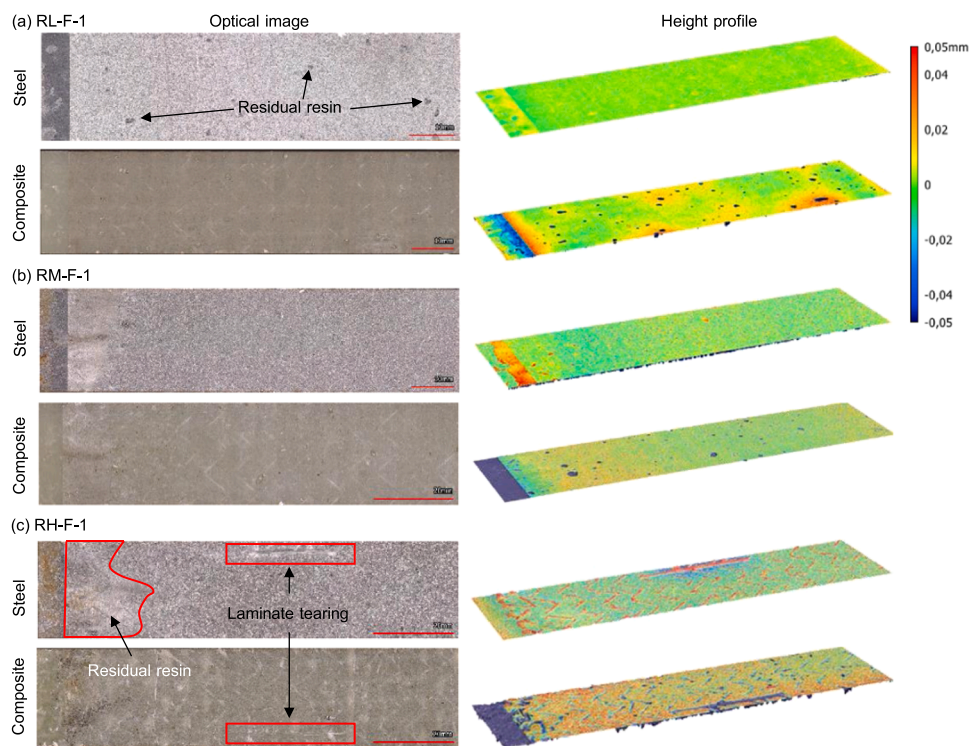

Fig. 17. Representative fracture surfaces of fatigue tested specimens.

remaining on the steel surface. The high roughness series experienced mixed adhesive failure and cohesive failure through thin layer of resin and limited through CSM. The fracture surfaces are more irregular, with a lot of resin and pieces of CSM remaining on the steel surface as shown in Fig. 17 (c) although much less than those under static tests. This means that the crack propagation occurs preferentially in the region of composite-to-steel interface under mode II cyclic loading. This difference between static and fatigue failure modes is also reported in literature [31,32], which stated that the fiber bridging effect is not pronounced for mode II interlaminar failure under cyclic loading.

5.2. Crack growth and SERR development

The variations of mode II SERR range of each specimen during the cyclic tests were calculated by the EGM and summarized in Fig. 18. The crack length measurements, determined by analysing the shear strains at the interface [31], is also shown. Results of specimen RL-F-3 were not obtained due to a malfunction of the DIC system during the test. It can be seen that results of each configuration are reproducible. The SERR decreases rapidly from the initial cycles and stabilizes gradually as the test continues. Specifically, the SERR values decreases from above 0.3 N/mm to a stabilized value of around 0.08 N/mm for low roughness series. The SERR range for the medium and high roughness series are higher. For the medium roughness series, the SERR range decreases from above 1 N/mm to a stabilized value of around 0.4 N/mm, while for high roughness series, the SERR range decreases from above 2.2 N/mm to a stabilized value of 0.5 N/mm. Driven by the SERR, the crack grows fast initially and stabilizes gradually towards the end. Tests were stopped
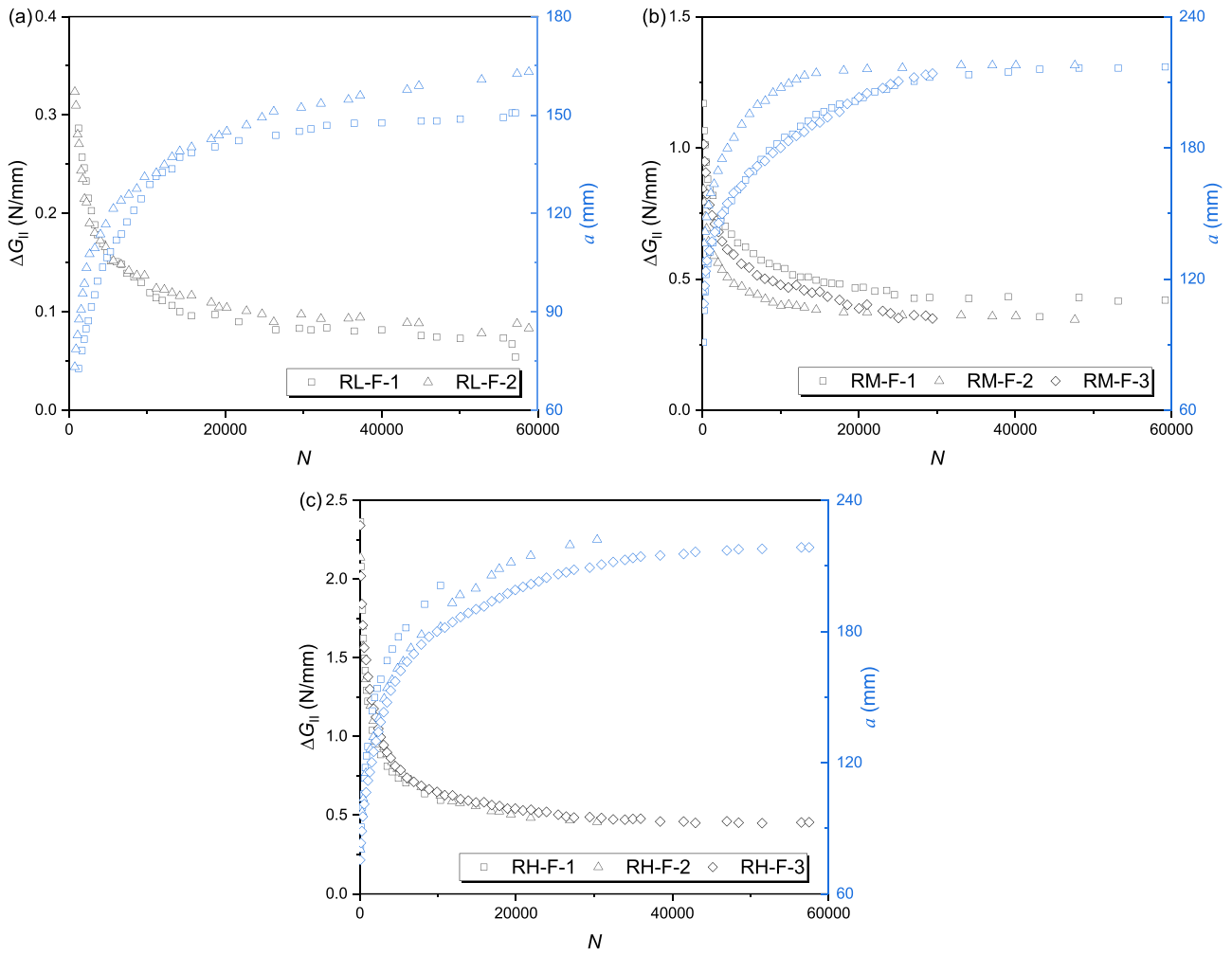
Fig. 18. Fatigue crack growth and mode II SERR development of (a) RL series, (b) RM series and (c) RH series.

when no further crack growth could be detected by the DIC system, except for the low roughness specimens where the crack growth stabilised at 165 mm. The crack growth for other two roughness series both stabilised at around 220 mm, corresponding to the location of the right loading point.

In order to consider influence of friction on SERR at the crack tip, FEA was performed as explained in Section 3, next to EGM, to calculate the mode II SERR at different force levels and crack lengths. Three series of models are built for specimens with different roughness, each of which is defined with the friction coefficient obtained by the 4 Hz friction tests described in Section 2.3 (see Fig. 5(d)). A relationship between the test force (P), the crack length (a) and the G_{II} was established, as shown in Fig. 19. A non-linear surface fit was applied to the numerical results using Eq. (10). The force term, P, is of second-order to be consistent with that in the EGM (see Eq. (4)). A linear correlation of the crack length, a, is included to take into account the geometrical non-linearity and friction effect [31] which cannot be considered by the EGM. Parameters k_1, k_2 and k_3 are determined by the least squares method and are listed in Table 5 for different roughness series. Substituting forces and crack lengths from the tests into Eq. (10), the mode II SERR with friction effect considered can be calculated. The calculated SERR based on the non-linear FEA will be used to establish the fatigue resistance curves.

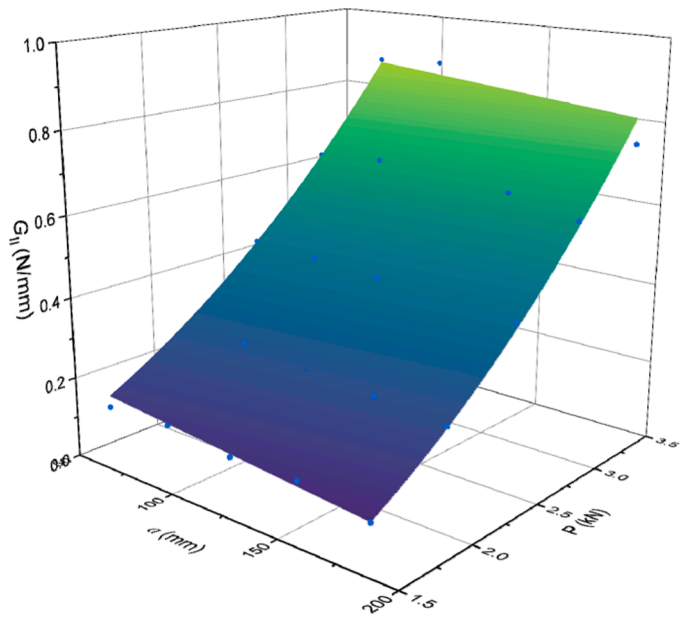$$G = k_1 P^2 + k_2 a + k_3 \tag{10}$$

Fig. 19. Mode II SERR vs. force and crack length from FEA.

5.3. Fatigue resistance curves

To construct the fatigue resistance curves, namely the Paris curves, the crack growth rate, da/dN, is calculated by the secant method recommended in [33], as shown in Eq. (11):

$$da/dN_{\bar{a}} = (a_{i+1} - a_i)/(N_{i+1} - N_i) \tag{11}$$

where i represents the ith data point. The average crack length in each crack increment, $\bar{a} = (a_{i+1} + a_i)/2$ is used to calculate the corresponding SERR. The crack growth rate is plotted against the ΔG_{II} calculated by EGM and FEA in Fig. 20 for each roughness series, and fitted by a power function as described in Eq. (12) such that the Paris curves can be obtained:

$$da/dN = C(\Delta G_{II})^m \tag{12}$$

where C and m are parameters determining the intercept and slope of the Paris curves, respectively. They were determined by the least squares method and listed in Table 6 for each specimen. It should be noted that data points corresponding to crack length above 200 mm are excluded in the Paris curves to eliminate the influence of compressive stresses resulting from the right loading point [27]. It can be seen from Fig. 20

Table 6
Paris curve parameters of different roughness series.

Specimen series	EGM			FEA with friction		
	C	m	C'	C	m	C'
RL-F	1.70	3.30	1.99	4.51	3.29	6.85
RM-F	0.04	3.97	0.051	0.14	3.97	0.15
RH-F	0.01	3.07	0.0078	0.03	3.47	0.03
Average	-	3.45	-	-	3.58	-

that data points from each roughness series are within a reasonable scattering range. Curves based on calculation of SERR by use of FEA (dashed lines) always shift towards the left compared to the EGM-based curves (solid lines). In case of the same slope parameter m the FEA-based results are reflected by the higher C values compared to EGM-based results as shown in Table 6. This difference is mainly related to the friction effect, as discussed in Section 4.3 and **Ref.** [31]. Friction forces at the fractured interface, as well as between the loading/supporting point and the specimen, contribute to load transfer mechanism of the specimen, leading to reduced portion of forces that need to be transferred at the crack tip and therefore reduced SERRs at the crack tip. This effect can be considered by a non-linear FE model but cannot be
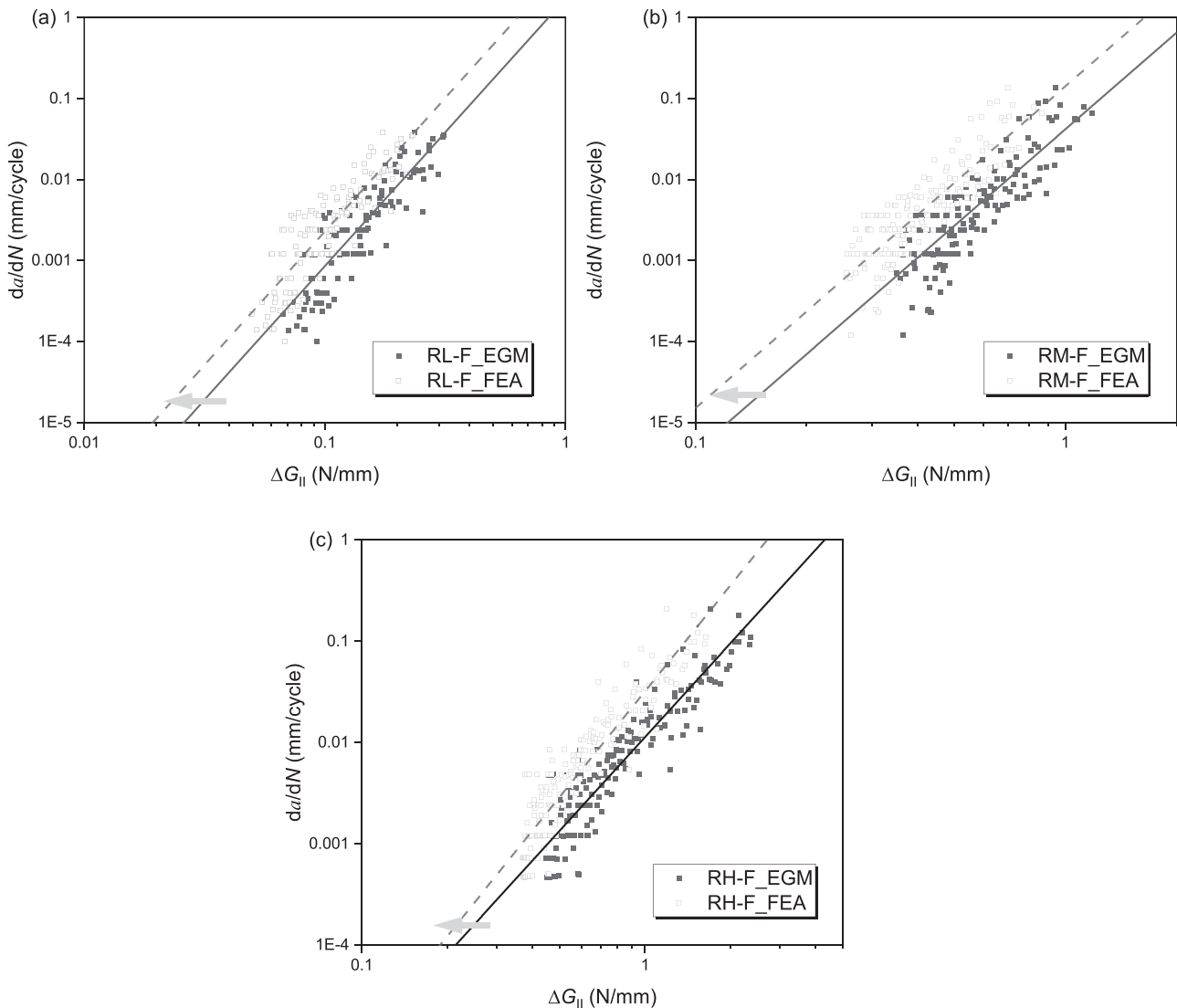

Fig. 20. Paris curves with SERR obtained by EGM and FEA from (a) RL series, (b) RM series and (c) RH series.

considered by the linear EGM method. By analysing the sets of FEA and EGM-based results, the pattern emerges at the bottom part of the Paris curves. Although the bottom part of the curve corresponds to an already developed crack, therefore larger fracture surface where friction could be exhibited, the contact stresses at the fractured and support/load faying surfaces are lower at the stage due to reduced load applied in the displacement controlled experiment. In total there is less friction at the stage of developed crack which is shown by a slightly smaller difference between the curves from EGM and FEA at the bottom of the Paris curves in Fig. 20.

Data points from all roughness series were plotted together for evaluating the effect of steel surface roughness, as shown in Fig. 21 (a) (based on EGM) and (b) (based on FEA). The critical SERRs are also indicated in these two figures for each roughness series based on EGM and FEA. The least squares method is used to fit the C and m values for each roughness independently (solid lines), which are listed in Table 6. It can be seen that, for both numerical and analytical methods, Paris curves from different roughness series are generally parallel, namely the slope of Paris curve, m, is mildly dependent, up to 20%, on the steel surface roughness. However, the position of the curves changes significantly among different roughness, with the C parameter decreasing up to two orders of magnitude as the roughness increases. This means that the crack growth rate of the high roughness series can be only 0.5–1% of the low roughness series at the SERR range of 1 N/mm. On the other hand, the fatigue resistance of RM series can be higher than that of the RH series at relatively low (e.g. below 0.1 N/mm) SERR ranges due to the higher curve slope (m value) of the RM series.

The m values are plotted against the roughness parameter S_q and S_{dr} in Fig. 22 (a) and (b), respectively. The variation of m is within an approximate range from 3.0 to 4.0 for EGM-based and FEA-based results, which is much smaller compared with the variation of magnitudes of the C parameter. Therefore, for further comparison of Paris curves from different roughness series, it is adopted that the m parameter is independent of the roughness levels. The average values of m for EGM and FEA based analysis are indicated in Table 6. The EGM-based m value overlaps well with the FEA-based result, despite the friction effect. The average values of m parameter, 3.45 and 3.58 for the EGM and FEA-based results respectively, are therefore taken and the C parameters are determined again for each series following the least squares method.

The new fitted Paris' curves are plotted as dash lines in Fig. 21. The newly obtained C parameters, C', are listed in Table 6 and are plotted against the roughness parameter S_q and S_{dr} in Fig. 23 (a) and (b), respectively. Compared with the initial C parameters, the new C' parameters change slightly due to the fixed m values. It can be seen from Fig. 23 that the C' parameter decreases as the roughness S_q and

developed area ratio S_{dr} increases. Generally speaking, the C' parameter becomes one order of magnitude lower when the roughness increases from the low level to the medium level, and also from the medium level to the high level. Considering the variation trend of C parameter, a power function, Eq. (13), is used to depict the relationship between C and roughness parameters:

$$C = q(S)^b \tag{13}$$

where S is the roughness parameter, S_q or S_{dr}, q and b are the fitted parameters, determined by the least squares method. The fitted results of q and b are listed in Fig. 23. Comparing results obtained from EGM and FEA, the FEA-based C parameters are higher than the EGM-based results. This is again due to the friction effect. Taking the friction at the interface and the support/load regions into account, the FEA-based Paris curves shift towards the left of the EGM-based curves as shown in Fig. 20, thus leading to apparently 'lower' fatigue resistance and higher C parameters.

Compared to the fracture toughness, fatigue resistance of the composite-to-steel bonded joints seems to be more sensitive to the surface roughness of the steel adherend. Taking the FEA-based results as an example, the crack propagation rate at $\Delta G_{II} = 1$ N/mm (represented by the C values) decreases by 98% from 6.85 mm/cycle to 0.15 mm/cycle when the roughness S_q increases by 2 times from the low to the medium roughness level. A 80% decrease of crack propagation rate is found when S_q increases by 50% from the medium to the high roughness level. A similar trend is also found when the roughness is expressed by S_{dr}. This means that the improvement of fatigue resistance comes essentially from a lager effective bonding area. The fatigue resistance is highly influenced by the roughness features on the steel surfaces possibly due to the fact that the adhesive failure is the predominate failure mode. This is different from **Ref.** [19], which stated that the fatigue performance is insensitive to the surface roughness when the crack path moved farther from the interface. However, it should be noted that in the current study the adhesive failure is forced by placing the steel adherend on the top in order to characterise the minimum possible fatigue resistance of the bi-material joints. In real application, such as in wrapped composite joints [35], fibre bridging may be exhibited thus the bi-material bonded joints could have higher fatigue resistance. Furthermore, the enhancing effect on the fatigue resistance does not show a decreasing trend at high roughness level, as observed for fracture toughness, indicating that the bonded joint is not effected by the same deterioration mechanisms as for the static performance. In conclusion, the results show that in the adverse case of adhesive failure, the fatigue resistance of the bonded joint can be sufficiently ensured as long as an appropriate surface preparation is applied before joining.
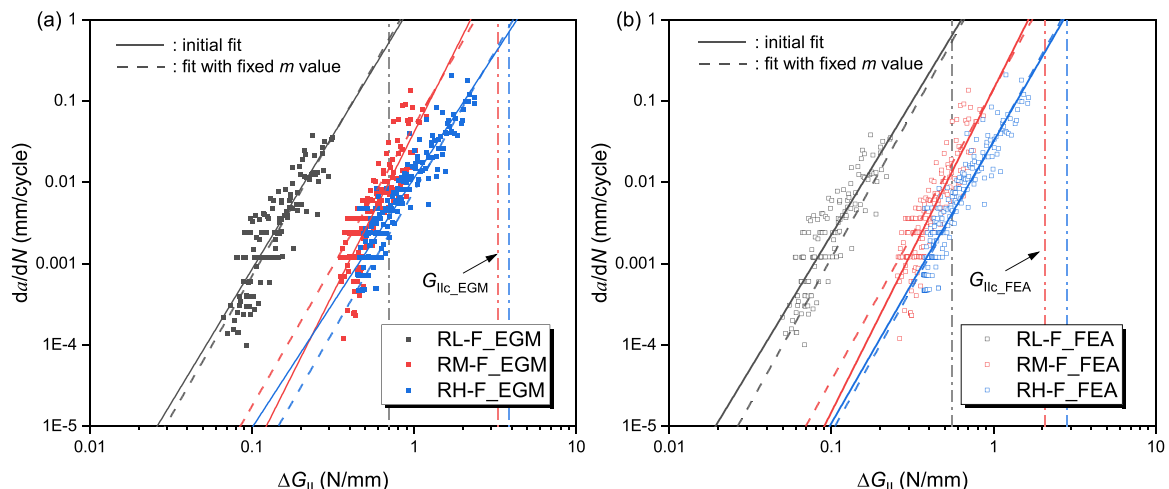

Fig. 21. Paris curves of different roughness with SERR obtained by (a) EGM and (b) FEA.
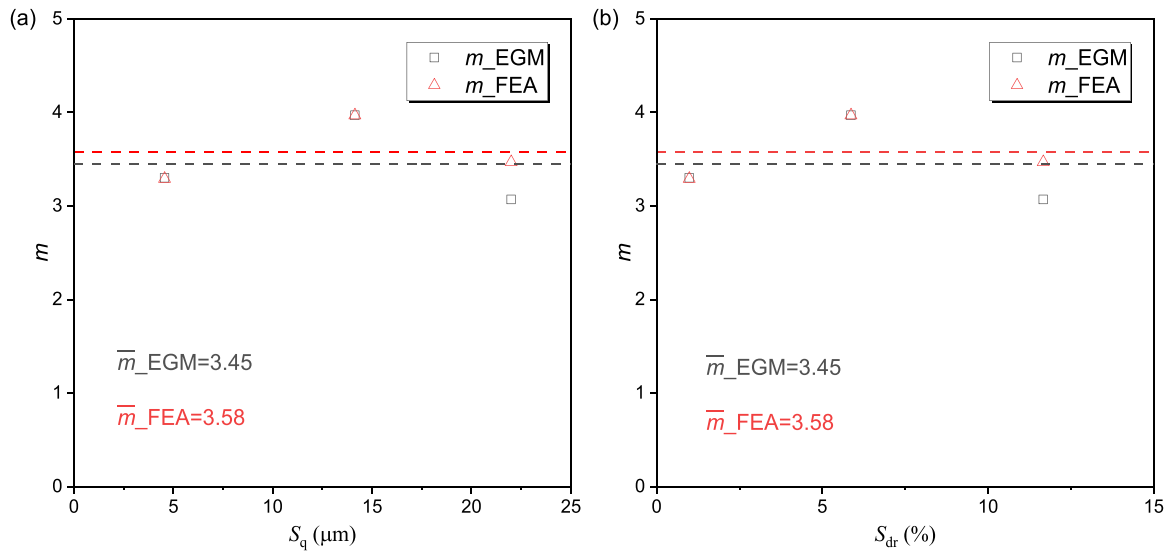
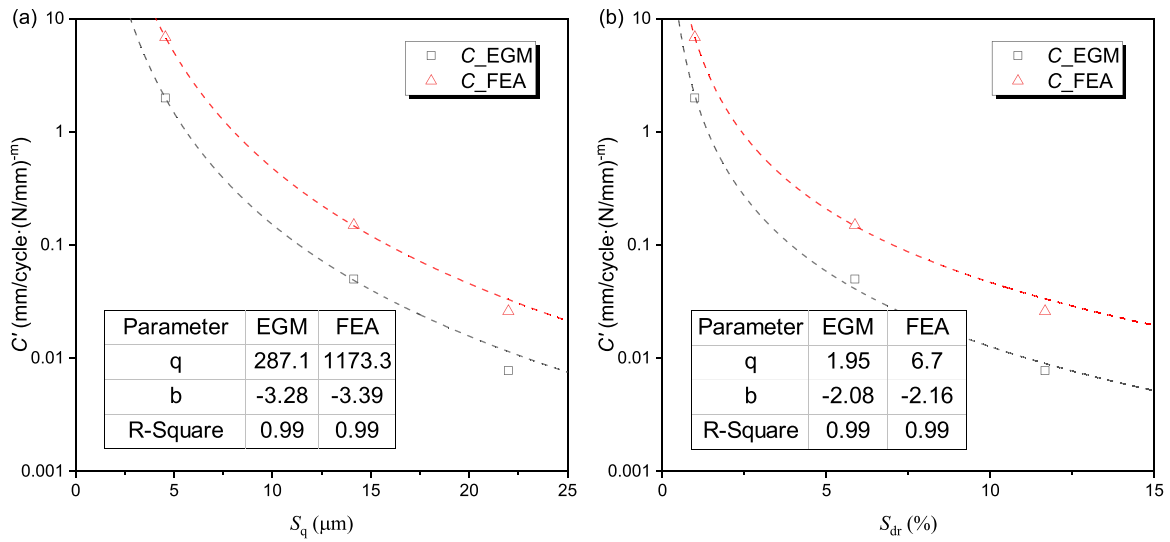**Fig. 22.** Influence of steel surface roughness on the *m* parameter expressed by (a) S_q and (b) S_{dr}.

Fig. 23. Influence of steel surface roughness on the C' parameter expressed by (a) S_q and (b) S_{dr}.

6. Conclusions

Understanding and quantifying the bond performance of the bi-material composite-to-steel interface, is of great importance for successful application of bonded joints in load-bearing structures. The bond quality is known to be sensitive to production tolerances with respect to surface preparation quality of the steel element but mildly quantified in current literature. The present study investigates the influence of the steel surface roughness on the mode II fracture toughness and fatigue crack growth properties of the bonded composite-to-steel interface, aiming to provide important information for predicting fracture behaviour and fatigue life of the joints. By performing quasi-static and fatigue 4ENF tests on three specimen series with surface roughness ranging from 5 μm to 22 μm, the following specific conclusions can be drawn:

- Under static loading, adhesive failure, directly at steel surface, prevails in specimens with low and medium surface roughness while fiber-tear failure with fiber bridging is evident in specimens with highest surface roughness leading to larger fracture toughness.

Correspondingly, initiation value of strain energy release rate increases by more than 2.8 times from low to medium toughness levels and only increase by 36% from medium to high roughness levels. The enhancing effect is mainly due to the enlarged effective bonding area between steel and composite as the roughness increases. Possible deterioration mechanisms such as voids formation may counteract this effect at highest roughness.

- In the case of fatigue loading, the low and medium roughness series are again characterized by adhesive failure while high roughness series experienced mixed adhesive and cohesive failure through thin layer of resin. Fatigue crack propagation is found to be following the Paris regime in the tested range of strain energy release rates. The slope of Paris curve, *m*, is mildly dependent, up to 20%, on the steel surface roughness and is around 3.58. However, the fatigue resistance of the bonded joint increases significantly as the roughness increases, with the *C* parameter decreasing one order of magnitude (6.85–0.15) from low to medium and another order of magnitude (0.15–0.03) from medium to high roughness. This is due to the fact that the crack path under fatigue loading is close to the interface and surface texture plays an important role. Thus, increasing the steel

roughness by surface preparation to the highest level does not bring large benefit for fracture bonding performance due to quasi-static loading but does have beneficial effect for fatigue performance due to cyclic load.

- The friction effects in 4ENF specimens can lead to higher calculated fracture toughness and fatigue resistance when employing the well-known analytical solution a.k.a. the extended global method. Specifically, the fracture toughness against quasi-static loading and crack propagation rate due to fatigue loading can be falsely characterized 60–70% optimistic (non-conservative) compared to more accurate estimation of the crack growth parameters by the virtual crack closure technique in finite element model.
- The presented work brings the method to take into account the friction effects into account by determining the strain energy release rates in the finite element model where friction at the insert and cracked interface between composites and steel are incorporated in a robust non-linear solution utilising Abaqus/Explicit dynamic solver. The friction coefficients are measured in tribometer tests with the testing frequency being 0.2 Hz and 4 Hz to mimic the quasi-static and fatigue loading cases, respectively. The friction coefficients are found to be approximately 0.25 and 0.5 for the PTFE insert region and cracked region regardless the steel surface roughness.

In conclusion, effective surface preparation of the steel adherend is essential to achieve enough sufficient roughness and enhance the fatigue resistance of the composite-to-steel bonded joints.

CRediT authorship contribution statement

Feng Weikang: Writing – original draft, Validation, Software, Methodology, Investigation, Formal analysis. **Arouche Marcio Moreira:** Writing – review & editing, Validation, Supervision, Methodology, Investigation. **Pavlovic Marko:** Writing – review & editing, Supervision, Project administration, Funding acquisition, Conceptualization.

Declaration of Competing Interest

The authors declare that they have no known competing financial interests or personal relationships that could have appeared to influence the work reported in this paper.

Data Availability

Data will be made available on request.

References

[1] An Introduction, in: A. Vlot, J.W. Gunnink (Eds.), Fibre Metal Laminates, Springer Netherlands, 2001, https://doi.org/10.1007/978-94-010-0995-9.

[2] M. Dlugosch, J. Fritsch, D. Lukaszewicz, S. Hiermaier, Experimental investigation and evaluation of numerical modeling approaches for hybrid-FRP-steel sections under impact loading for the application in automotive crash-structures, Compos Struct. 174 (2017) 338–347, https://doi.org/10.1016/J.COMPSTRUCT.2017.04.077.

[3] X.L. Zhao, L. Zhang, State-of-the-art review on FRP strengthened steel structures, Eng. Struct. 29 (2007) 1808–1823, https://doi.org/10.1016/j.engstruct.2006.10.006.

[4] D. Borrie, S. Al-saadi, X.L. Zhao, R.K. Singh Raman, Y. Bai, Bonded cfrp/steel systems, remedies of bond degradation and behaviour of CFRP repaired steel: An overview, Polym. (Basel) 13 (2021), https://doi.org/10.3390/POLYM13091533.

[5] P. Colombi, Reinforcement delamination of metallic beams strengthened by FRP strips: fracture mechanics based approach, Eng. Fract. Mech. 73 (2006) 1980–1995, https://doi.org/10.1016/j.engfracmech.2006.03.011.

[6] M. Bocciarelli, P. Colombi, G. Fava, C. Poggi, Prediction of debonding strength of tensile steel/CFRP joints using fracture mechanics and stress based criteria, Eng. Fract. Mech. 76 (2009) 299–313, https://doi.org/10.1016/j.engfracmech.2008.10.005.

[7] W. Feng, M. Pavlovic, Fatigue behaviour of non-welded wrapped composite joints for steel hollow sections in axial load experiments, Eng. Struct. 249 (2021), 113369, https://doi.org/10.1016/J.ENGSTRUCT.2021.113369.

[8] P. He, M. Pavlovic, Failure modes of bonded wrapped composite joints for steel circular hollow sections in ultimate load experiments, Eng. Struct. 254 (2022), 113799, https://doi.org/10.1016/j.engstruct.2021.113799.

[9] G. Lucchetta, F. Marinello, P.F. Bariani, Aluminum sheet surface roughness correlation with adhesion in polymer metal hybrid overmolding, CIRP Ann. - Manuf. Technol. 60 (2011) 559–562, https://doi.org/10.1016/j.cirp.2011.03.073.

[10] S. Zhang, R. Panat, K.J. Hsia, Influence of surface morphology on the adhesion strength of epoxy–aluminum interfaces, J Adhes Sci Technol 17 (2012) 1685–1711, https://doi.org/10.1163/156856103322396749.

[11] J.P.B. van Dam, S.T. Abrahami, A. Yilmaz, Y. Gonzalez-Garcia, H. Terryn, J.M.C. Mol, Effect of surface roughness and chemistry on the adhesion and durability of a steel-epoxy adhesive interface, Int J. Adhes. Adhes. 96 (2020), 102450, https://doi.org/10.1016/j.ijadhadh.2019.102450.

[12] D. Zhang, Y. Huang, Influence of surface roughness and bondline thickness on the bonding performance of epoxy adhesive joints on mild steel substrates, Prog. Org. Coat. 153 (2021), 106135, https://doi.org/10.1016/J.PORGCOAT.2021.106135.

[13] Smith K.R. Correlating Fracture Toughness and Surface Roughness for a Ductile Epoxy Adhered to Aluminum Substrates. University of Tennessee, 2021.

[14] J.H. Hwang, C.K. Jin, M.S. Lee, S.W. Choi, C.G. Kang, Effect of surface roughness on the bonding strength and spring-back of a CFRP/CR980 hybrid composite, Metals 8 (2018) 1–12, https://doi.org/10.3390/met8090716.

[15] M. Moreira Arouche, S. Teixeira de Freitas, S. de Barros, On the influence of glass fiber mat on the mixed-mode fracture of composite-to-metal bonded joints, Compos Struct. 256 (2021), 113109, https://doi.org/10.1016/J.COMPSTRUCT.2020.113109.

[16] P. Kumar, P.S. Shinde, G. Bhoyar, Fracture toughness and shear strength of the bonded interface between an aluminium alloy skin and a FRP patch, J. Inst. Eng. Ser. C. 100 (2019) 779–789, https://doi.org/10.1007/s40032-018-0467-1.

[17] M.A.G. Silva, H. Biscaia, P. Ribeiro, On factors affecting CFRP-steel bonded joints, Constr. Build. Mater. 226 (2019) 360–375, https://doi.org/10.1016/j.conbuildmat.2019.06.220.

[18] J. Ou, Y. Shao, C. Huang, X. Bi, Bond behavior of CFRP sheets-to-steel shear joints with different steel surface treatments, Compos Struct. 322 (2023), 117376, https://doi.org/10.1016/j.compstruct.2023.117376.

[19] S. Azari, M. Papini, J.K. Spelt, Effect of surface roughness on the performance of adhesive joints under static and cyclic loading, J. Adhes. 86 (2010) 742–764, https://doi.org/10.1080/00218464.2010.482430.

[20] K. Shikimoto, S. Ishida, W. Jinnouchi, Y. Ogawa, H. Akebono, A. Sugeta, Effect of laser patterning preprocessing on fatigue strength of adhesive bonded joints using thin steel plate, Mater. Trans. 61 (2020) 469–474, https://doi.org/10.2320/matertrans.Z-M2019870.

[21] A. Manoli, R. Ghadge, P. Kumar, Effect of surface roughness on the fatigue strength of E-glass composite single lap joint bonded with modified graphene oxide-epoxy adhesive, Mater. Phys. Mech. 51 (2023) 65–80, https://doi.org/10.18149/MPM.5122023_7.

[22] B. Carrera, Effects of Surface Condition on the Fatigue Behavior of CFRP-to-Steel Joints, Virginia Polytechnic Institute and State University, 2022.

[23] W. Wang, S.T. De Freitas, J.A. Poulis, D. Zarouchas, A review of experimental and theoretical fracture characterization of bi-material bonded joints, Compos Part B Eng. 206 (2021), 108537, https://doi.org/10.1016/j.compositesb.2020.108537.

[24] ISO 6892-1:2016. Metallic materials - Tensile testing - Part 1: Method of test at room temperature n.d. European Committee for Standardization, 2016.

[25] ISO-527-1. Plastics - Determination of tensile properties Part 1: General principles. ISO International Organization for Standardization, Geneva, Switzerland, 2019.

[26] ISO/DIS-14126. Fibre-reinforced plastic composites - Determination of compressive properties in the in plane direction, ISO International Organization for Standardization, Geneva, Switzerland, 2022.

[27] ISO-14129. Fibre-reinforced plastic composites - Determination of the in-plane shear stress/shear strain response, including the in-plane shear modulus and strength, by the plus or minus 45 degree tension test method, ISO International Organization for Standardization, Geneva, Switzerland, 1997.

[28] ISO 25178–2:2021(en), Geometrical product specifications (GPS) — Surface texture: Areal — Part 2: Terms, definitions and surface texture parameters n.d. ISO International Organization for Standardization, Geneva, Switzerland, 2021.

[29] P.J. Blau Friction science and technology: From concepts to applications, second edition. 2008.

[30] M.M. Arouche, W. Wang, S. Teixeira de Freitas, S. de Barros, Strain-based methodology for mixed-mode I+II fracture: a new partitioning method for bi-material adhesively bonded joints, J. Adhes. 95 (2019) 385–404, https://doi.org/10.1080/00218464.2019.1565756.

[31] W. Feng, M. Moreira Arouche, M. Pavlovic. Fatigue crack growth characterization of composite-to-steel bonded interface using ENF and 4ENF tests. Submitted 2023.

[32] M. Shahverdi, A.P. Vassilopoulos, T. Keller, Mixed-Mode I/II fracture behavior of asymmetric adhesively-bonded pultruded composite joints, Eng. Fract. Mech. 115 (2014) 43–59, https://doi.org/10.1016/j.engfracmech.2013.11.014.

[33] J.G. Williams, On the calculation of energy release rates for cracked laminates, 362 1988, Int J. Fract. 36 (1988) 101–119, https://doi.org/10.1007/BF00017790.

[34] M. Zhu, L. Gorbatikh, S. Fonteyn, D. Van Hemelrijck, L. Pyl, D. Carrella-Payan, et al., Digital image correlation assisted characterization of Mode I fatigue

delamination in composites, Compos Struct. 253 (2020), 112746, https://doi.org/10.1016/j.compstruct.2020.112746.

[35] W. Feng, M.Pavlovic. P. He, Interfacial fatigue debonding retardation in wrapped composite joints: experimental and numerical study, Compos Struct. 319 (2023), 117146, https://doi.org/10.1016/j.compstruct.2023.117146.